Supplementary information

Ultra-Coherent Meta-Emitter Tailors Arbitrary Thermal Wavefront

Contents:

Supplementary Note:

Supplementary Figures:

Supplementary Tables:

Supplementary Movie:

Supplementary Notes

S.1 Difficulites in complex thermal wavefront emission

S1.1. Comparison of different reported approaches and our work

Coherence enhancement of thermal emission relies on the long-range resonances along the emission surface. These nonlocal resonances can arise from material-based (internal) mechanisms, such as surface phonon polaritons (SPhPs)[1–3] in polar materials within the Reststrahlen band or surface plasmon polaritons (SPPs)[4,5] in metals around the plasma frequency, or from external resonances supported by carefully designed structures[6–12]. On the other hand, complex emission wavefront is attributed by structural entropy[13], which requires sufficient degrees of freedom in structure variation to tailor the scattering phase.

In the case of material resonances, these resonant surface modes correlate emission behavior over distances comparable to the propagation length of the traveling wave. Although the resonance itself is independent of the structure, seemingly offering freedom in structural design, the emission phase in source-emitter coupled systems remains highly sensitive to the wavevector of the surface wave. Thermal populated surface wave possess arbitrary in-pane wavevector directions, which significantly disrupt the emission profile. In the one-dimensional grating case, thermal wavefronts generated by waves with opposite wavevector directions are typically treated as reciprocal processes[3,14], which can partially achieve thermal focusing in theory, but suffer from strong reciprocal wavefront noise[3]. Moreover, such architectures often exhibit dispersion within resonance band, leading to a “rainbow effect”[1,4,5] in plane wave emission and large background noises in more complex wavefront emission.

For the external resonances, spatiotemporal coherence can be engineered through resonance mode design. For a specific mode, different dispersion band region can be selected for thermal emission based on critical coupling condition[15]. For the intraband region, travelling wave behavior dominates, which still faces issues related to reciprocal events and dispersion noises[6–8], similar to those described cases above. Alternatively, weakly dispersive bandedge mode can provide specific scattering phases for individual elements. Combined with symmetry-separated local mode modulation, Alù *et al*. recently proposed a compound thermal metasurface architecture that theoretically supports complex coherent functionalities[14] and experimentally demonstrated asymmetric unidirectional emission[16]. Unlike traveling wave modes, the bandedge modes correlate the neighboring resonators via evanescent fields, with the spatial coherence govern by the coupling strength (κ) between them. A larger coupling coefficient enhances spatial coherence, but also makes its resonance behavior highly sensitive to the structural variations, leading to a significant band splitting under applied local perturbations, manifesting as additional lattice modes in their experiment. The relationship among band splitting ($\Delta\omega$), spatial coherence (L_c) and coupling strength (κ) is derived by spatial coupled mode theory in the following two subsections (S1.2, S 1.3).

This trade-off between high coherence (typically requiring periodic structures) and strong wavefront manipulation capability (requiring aperiodic designs) can be mitigated by separating the sources and emitter, thereby decoupling the resonances to the emission elements. By localizing the source into a single unit in an array, Yu, et al. proposed a resonantly coupled mesoscopic emitter network to address the wavevector uncertainty along the emission surface, which can theoretically achieve self-focusing thermal emission and holography[12]. Unfortunately, the single-source requirement poses challenges for position-dependent absorptive-structural fabrication, single-point heating excitation, and it also suffers from the weak emission power in detection, making experimental realization difficult.

Due to these limitations, although extensive efforts have been made to enhance the coherence of the thermal radiation, all the experimental demonstrations to date have been limited to plane-wave emission. More complex wavefront emissions, such as thermal focusing and holography, remain theoretical concepts, as listed in Supplementary Table1.

Our proposed meta-emitter incorporates synergistically coupled lossy and lossless outer boundaries, enabling complex thermal wavefront manipulation capability without sacrificing the signal-to-noise ratio or the emission power, which can experimentally demonstrate this fascinating thermal wavefront control phenomenon. The connecting tunnel serves as an effective coherent source, fixing the scattering phase on the lossless funnel, similar to the point source in Ref. 12. This thermal wavefront manipulation capability comes from the increased structural complexity.

Although our architecture looks like the cascading of different components together to achieve the desired functionality, which is similar to the traditional case, including spatial filter, spectral filter, polarizer and phase plate, as shown in Supplementary

Fig.1a. The underlying physics is distinctly different. In conventional thermal optical system, all the components are applied in the far-field, where most of energy is wasted during each filtering process. For our meta-emitter, all the processes are done in the near-field, which the energy can well optimized to couple to each other. The thickness of our design is about $1\lambda_0$, which is similar to the conventional thermal metasurfaces. Furthermore, similar to standard thermal metasurfaces, the bottom surface in our design also hosts fluctuating thermal sources, populated through the same physical mechanism. The key distinction is that this energy is guided through a central resonant tunnel and subsequently scattered into free space, enabling engineered coherence and tailored wavefronts within a unified thermal-emission framework.

In addition, the achromatic wavefront-shaping behavior enabled by the out-of-plane wavevector dispersion in the resonant tunnel—discussed in Fig. 3c–d of the Main Text and Supplementary Note S4—is another unique feature of our design. This property allows a broader spectral range to contribute to the desired wavefront, thereby enhancing energy utilization efficiency.

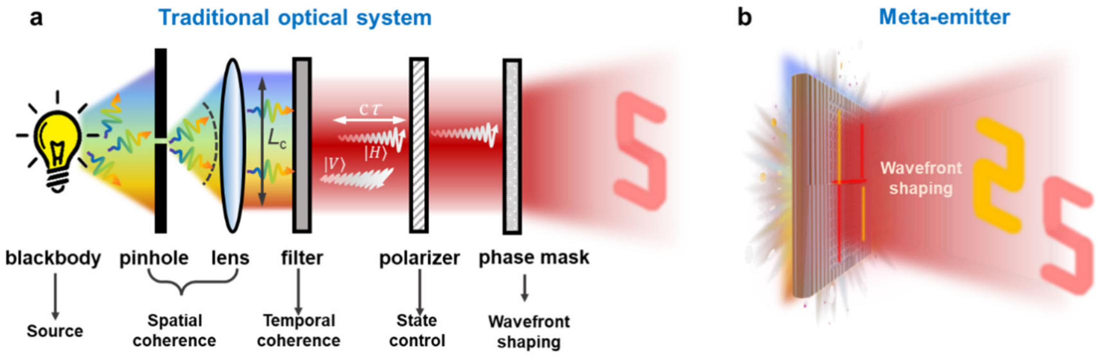

Supplementary Fig.1 The comparison of the traditional optical system and our meta-emitter in thermal wavefront shaping. a. Traditional system relies on spatial, spectral, polarization filter and phase plate to get wanted thermal wavefront. b. Meta-emitter integrates all these functions together to get the desired thermal wavefront.

S1.2. Spatial coherence of the band edge mode

The nanostructure array can be approximately regarded as a truncated waveguide array, whose dispersion behavior can be analyzed using spatial coupled mode theory (SCMT). For simplicity, we consider a one-dimensional waveguide array with a lattice period of Λ, as schematically illustrated in Supplementary Fig.2a. The dynamic evolution of the mode is described by the equation:

$$\frac{\mathrm{d}a_m(z)}{\mathrm{d}z} = i(\beta_0 + i\alpha)a_m(z) + i\beta_0\kappa[a_{m-1}(z) + a_{m+1}(z)], \tag{S1}$$

where a_m is the complex modal amplitude of m^{th} structure in the array as a function of z, β_0 and α are the propagation constant and decay rate of the mode at its eigenfrequency, and κ is the coupling coefficient between neighboring structures. For simplicity, only coupling from neighboring structures is considered herein.

Bloch's theorem sets a fundamental constraint on the wavefunction between neighboring structures:

$$a_{m+1} = a_m e^{iK\Lambda}, \qquad a_{m-1} = a_m e^{-iK\Lambda} \tag{S2}$$

Where $K \in [-\pi/\Lambda,\ \pi/\Lambda]$ is the in-plane (Bloch) wavevector, which characterizes the phase correlation between adjacent lattices. Applying the harmonic propagation solution $e^{i\beta z}$ and Eq. S2 to Eq. S1, the dispersion relationship is derived as:

$$i\beta = i(\beta_0 + i\alpha) + i\beta_0\kappa(e^{iK\Lambda} + e^{-iK\Lambda}), \tag{S3}$$

which simplifies to: $\beta = (\beta_0 + i\alpha) + 2\kappa\beta_0\cos(K\Lambda)$.

Under weak effective index ($\mathrm{n_{eff}}$) dispersive approximation, we have $\beta_0 = \mathrm{n_{eff}}\frac{\omega_0}{c}$, and $\beta = \mathrm{n_{eff}}\frac{\omega}{c}$ (with c is the light speed), allowing dispersion relationship to be rewritten as:

$$\omega = (\omega_0 + i\alpha\mathrm{n_{eff}}) + 2\kappa\omega_0\cos(K\Lambda), \tag{S4}$$

Based on the Lorentzian profile of resonance:

$$\mathrm{S}(\omega) \propto \frac{1}{(\omega-\omega_0)^2+\alpha^2}, \tag{S5}$$

The dispersion diagram can be constructed, as drawn in Supplementary Fig.2b.

The spatial coherence L_c (nonlocality length) of the band edge mode can be skimpily expressed as[14,16]:

$$L_\mathrm{c} = \sqrt{b\tau}, \tag{S6}$$

where τ is the mode lifetime (proportional to 1/α). Coefficient b is the band curvature at the band edge, which can be derived by the dispersion relationship in Eq. S4:

$$b(K=0) = \frac{d^2\omega}{dK^2}|_{K=0} = 2\omega_0\kappa\Lambda^2\cos(K\Lambda)\,|_{K=0} = 2\omega_0\kappa\Lambda^2, \tag{S7}$$

Substituting Eq. S7 into Eq. S6 yields:

$$L_\mathrm{c} = \Lambda\sqrt{2\omega_0\kappa\tau} = \Lambda\sqrt{2\kappa Q} \tag{S8}$$

Where Q = $\omega_0\tau$ is the quality factor of the resonance. The relation aligns with the underlying physics: a larger coupling strength κ results in a larger band curvature and enhanced spatial coherence.

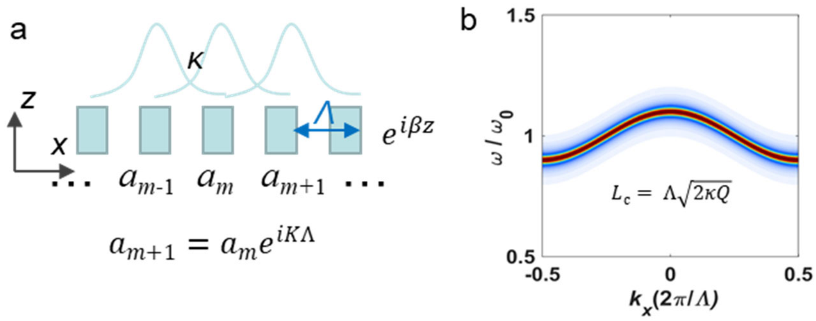

Supplementary Fig.2. Coupled mode theory of periodic waveguide array. a. Schematic diagram of periodic structures. b. Dispersion diagram of the resonance.

S1.3. Perturbation induced spectrum splitting

The wavefront shaping need local scattering manipulation of the extended mode, which can be treated as a local perturbation for the resonant structures. For an emission beam with a specific output angle, the perturbation distribution exhibits a large period. As drawn in Supplementary Fig.3a, for a super lattice composed of *N* unit cells with periodicity *L* = *NΛ*, Bloch's theorem evolves into:

$$a_{m+N} = a_m e^{iKN\mathrm{L}}, \tag{S9}$$

Here, $K \in [-\pi/NL,\ \pi/NL]$ is the superlattice Bloch wavevector, which characterizes the phase correlation between adjacent superlattices.

The coupling coefficient between the nth and (n+1)th cell acquires a Bloch phase factor:

$$\kappa_{n,n+1} = \kappa_1 e^{iK\Lambda},\ \kappa_{n,n+2} = \kappa_2 e^{iK2\Lambda}, \tag{S10}$$

where κ_1 and κ_2 are coupling strength of the adjacent and the next adjacent structures, respectively. This phase factor ensures the Hamiltonian satisfies translational symmetry over the super lattice period *L*.

Let $\mathbf{A} = [a_1, a_2, \dots, a_N]^T$ denote the modal amplitudes of the *N* cells in a superlattice. The coupled-mode dynamics are governed by:

$$\frac{d}{dz}\boldsymbol{A} = (i\beta_0\mathbf{B} - \boldsymbol{\Gamma})\boldsymbol{A}, \tag{S11}$$

Where $\mathbf{B}$ is the propagation constant matrix, containing intrinsic propagation constant and couplings:

$$\mathbf{B} = \begin{bmatrix} \beta_1 & \kappa_1 e^{iKa} & \kappa_2 e^{iK2a} & \dots & \kappa_1 e^{-iKa} \\ \kappa_1 e^{-iKa} & \beta_2 & \kappa_1 e^{iKa} & \dots & \kappa_2 e^{-iK2a} \\ \kappa_2 e^{-iK2a} & \kappa_1 e^{-iKa} & \beta_3 & \dots & 0 \\ \vdots & \vdots & \vdots & \ddots & \kappa_1 e^{iKa} \\ \kappa_1 e^{iKa} & 0 & \cdots & \kappa_1 e^{-iKa} & \beta_N \end{bmatrix}, \tag{S12}$$

where β_n is the normalized propagation constant of the *n*-th cell. The decay matrix $\boldsymbol{\Gamma}$

describs absorption losses:

$$\mathbf{\Gamma} = \begin{bmatrix} \gamma_1 & 0 & \dots & 0 \\ 0 & \gamma_2 & \dots & 0 \\ \vdots & \vdots & \ddots & \vdots \\ 0 & 0 & \dots & \gamma_N \end{bmatrix}, \tag{S13}$$

where γ_n is the decay rate of the n-th cell. For simplicity, the perturbation-induced propagation constant difference between neighboring structures is assumed equal :

$$\beta_0(\,\beta_\mathrm{n} - \beta_{\mathrm{n}-1}) = \Delta\beta. \tag{S14}$$

Substituting the harmonic solution $e^{i\beta z}$ and Eq. S10 into Eq. S11, we can obtain the dispersion relationship:

$$[\mathrm{i}(\beta - \beta_0\mathbf{B}) - \mathbf{\Gamma}]\boldsymbol{A} = 0, \tag{S15}$$

with weak effective index ($\mathrm{n_{eff}}$) dispersive approximation($\beta_0 = \mathrm{n_{eff}}\frac{\omega_0}{c},\ \beta = \mathrm{n_{eff}}\frac{\omega}{c}$), Eq. S15 can be rewritten as:

$$[\mathrm{i}(\omega - \omega_0\mathbf{B}) - \mathrm{n_{eff}}\mathbf{\Gamma}]\boldsymbol{A} = 0, \tag{S16}$$

For the *N* = 2, eigenfrequencies are:

$$\omega = \ \omega_0 \pm \sqrt{\Delta^2 + (2\omega_0\kappa)^2} - i\gamma, \tag{S17}$$

where $\Delta = \ \Delta\beta c/\mathrm{n_{eff}}$ is the perturbation strength. In the weak perturbation, strong coupling regime ($\Delta \ll 2\omega_0\kappa$), the splitting simplifies to:

$$\Delta\omega \approx 2\omega_0\kappa, \tag{S18}$$

The dispersion of the superlattice with N = 2, 3 and 10 are respectively presented in Supplementary Fig.3b-d. Due to the band folding effect, single band splits into multiple branches, which disturb emission performance.

As $N \to \infty$, subband density increases, approaching a quasi-continuum band. The perturbation effect averages out as an additional loss (nonradiative loss, originated from the imperfection fabrication) in the decay matrix, broadening the band and degrading spatial coherence.

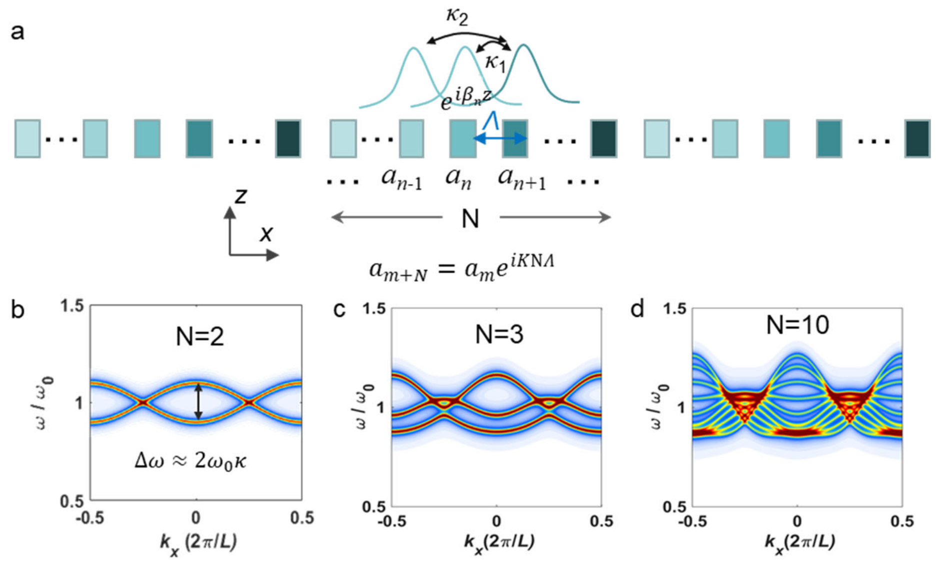

Supplementary Fig.3. Dispersion relationship for the perturbated periodic structures. a. Schematic of a superlattice containing N cells. b-d. Dispersion diagram for superlattices with $N\ =\ 2$, 3 and 10, respectively. Parameters: $\gamma = 0.01$; $\kappa_1 = 0.05$; $\kappa_2 = 0.001,\ \Delta\beta = 0.001/N$.

S.2 Examples of spatial coherence enhancement by enlarging group velocity

In the Main Text, we get the conclusion of surface mode's spatial coherence can be extended by enlarging its group velocity. The temporal coherence just sets an upper boundary of the spatial coherence ($L_c = c\tau$, where c is the light speed in free space), different spatial coherences can be obtained with the same temporal coherence by modifying the slope of the operational band. One representative extreme case is the comparison between our work and previously reported nonlocal thermal metasurfaces operating at the band edge. In Ref. 16, nonlocal thermal metasurfaces with a Q factor of 128 achieved a spatial coherence of only $1.6\lambda_0$. In this case, band variation within a narrow spectral width cannot longer be captured by the band slop (group velocity) any more, higher order of polynomial terms, such as band curvature ($b \propto\ d^2\omega/d\beta^2$), need to be applied. In contrast, our design, despite having a moderate Q factor of ~30 (the inset of Fig. 3h in the Main Text), achieves a spatial coherence of ~$11\lambda_0$, which is almost one order of magnitude higher than their work.

To further illustrate the role of group velocity, we designed two output surface modes with comparable temporal coherence but different group velocities at the operational frequency, as shown in Supplementary Fig.4a. The cross-spectral density components $W_{zz}(\rho)$ of the two modes as a function of ρ at a fixed height $z_0 = \lambda_0/10$ above the surface are plotted in Supplementary Fig.4b. Although Mode 2 has a slightly larger temporal coherence than Mode 1, the $W_{zz}(\rho)$ attenuates faster than Mode 1. The $1/\sqrt{e}$ correlation lengths of the W_{zz} are around $42\lambda_0$, $26\lambda_0$ for Mode 1and Mode 2, respectively, which is close to the $\tau \cdot v_g$ expectation ($40\lambda_0$,$28\lambda_0$for Mode 1and Mode 2, respectively). The slightly variation between the full-wave simulation and theoretical analysis comes from the near-field fluctuation of the surface wave.

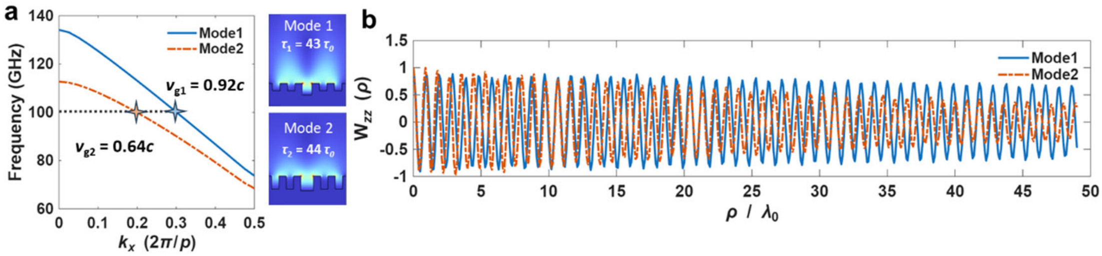

Supplementary Fig.4 Spatial coherence of surface modes with similar lifetime but different band slop. a. Dispersion properties of two surface modes. The |**E**|-profiles of eigenmodes are shown in the right panel. The corresponding group velocities and lifetimes are marked in the plot. b. Cross-spectral density component $W_{zz}(\rho)$ of the surface wave as a function of ρ at fixed height $z_0 = \lambda_0/10$ above the surface.

The cross-spectral density component $W_{zz}(\rho)$ of the surface wave is calculated by the method provided in Method section (Calculation of the cross-spectral density component W_{zz}) in the main text. The space-frequency dependent real parts of E_z components for the discussed three modes in the main text are drawn in Supplementary Fig. 5a-c, respectively. Cross-correlation function of E_z for these modes at a different spatial interval at presented in Supplementary Fig. 5d-e.

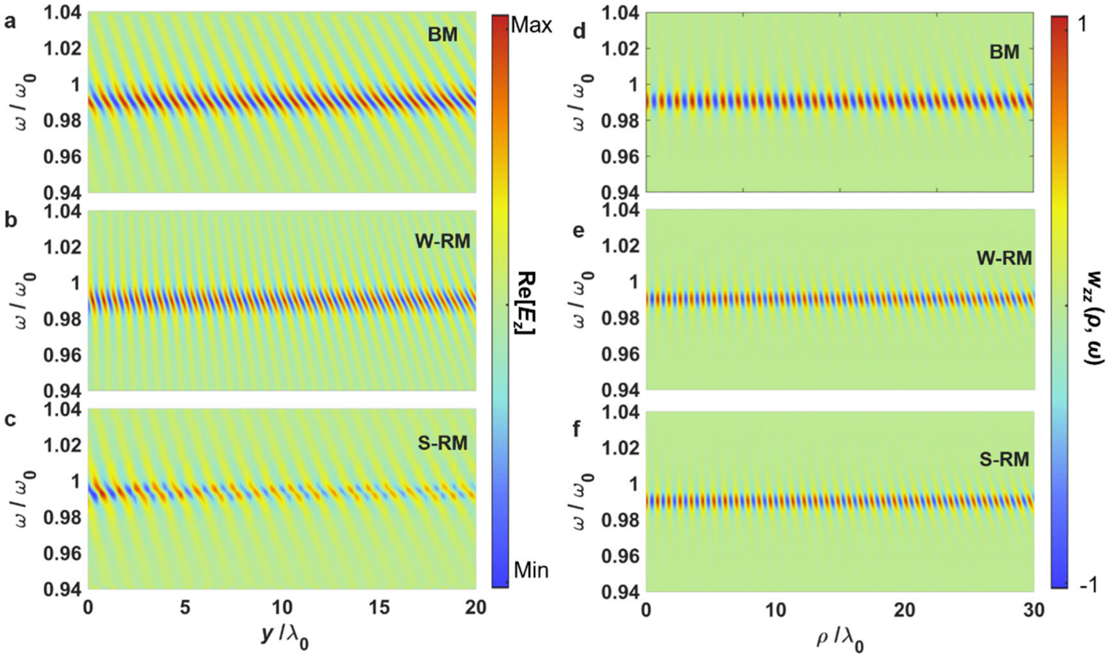

Supplementary Fig.5. Calculation of cross-spectral density component *Wzz*. a-c. The space-frequency dependent real part of the E_z component (above the top surface at $z = \lambda_0/10$) for BM, W-RM and S-RM, respectively. d-f. The real part of cross-correlation function w_{zz} of $E_z(0, \omega)$ and $E_z(\rho, \omega)$ for the above three modes, respectively.

At last, the temporal coherence is assumed as the same in the above discussion, it is variant in the realistic design. The band edge mode forms a standing wave, typically supporting a higher Q-factor (temporal coherence). The variation of spatial coherence needs to consider the mutual influence of temporal coherence and group velocity of the specific mode. In the previous study, the highest spatial coherence usually occurs at off-Γ point, which the Q-factor is not the highest point in the whole band[1,10,17].

The band diagram of each mode in Fig. 2f in the Main Text with light lines are plotted in Supplementary Fig.6.

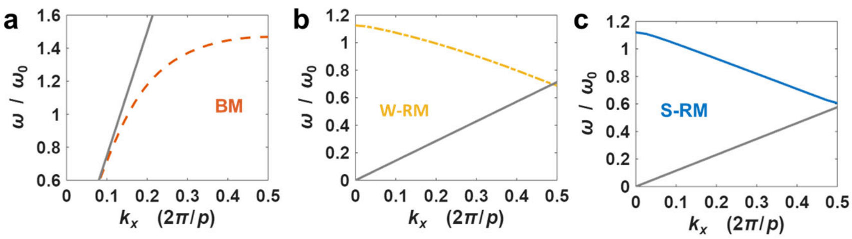

Supplementary Fig.6 The band diagrams of BM, W-RM and S-RM with light line. BM is dark mode which under the light line, and two radiation modes (W-RM and S-RM) are above the light line.

S.3 Energy tunneling efficiency calculation and optimization strategy discussion

S 3.1 Energy tunneling efficiency calculation

Due to the similarity of our design and classical extraordinary light transmission (EOT) architecture, we provide a brief discussion on the differences between the two schemes regarding the efficiency definition and possible optimization strategies. The energy transfer efficiency definition is different from previous cases due to the excitation differences. In EOT systems, a coherent plane wave source is applied. The transmission efficiency can be directly defined as the ratio of transmitted power to the incident power ($\eta = P_{\mathrm{trans}}/P_{\mathrm{inci}}$), measurable via a Vector Network Analyzer (VNA) for the microwave band or a spectrometer in the optical band. In our case, however, the excitation originates from stochastic thermal fluctuations. The total transmitted energy strongly depends on the dipole position and polarization, making direct quantification difficult. Therefore, we used the surface mode as the reference source and defined the coupling efficiency as the ratio of the energy carried by the top surface mode after tunneling through the slit to that of the bottom surface mode. This measures the mode-to-mode transfer efficiency through the three coupled components: bottom surface waveguide, slit waveguide, and top radiation surface.

We performed simulations in COMSOL Multiphysics as illustrated in Supplementary Fig.7a. The size of the simulated structure is ~46λ_0 long. A dipole source is placed at one edge of the bottom surface (~22λ_0 from the slit) to excite the bottom surface mode. The incident energy (P_{in}) from the bottom surface mode is calculated by integrating energy ~20λ_0 away from the excitation dipole, where the slit is removed, as shown in Supplementary Fig.7b. For the full structure, three top surface configurations (Bottom: BM; top: BM, W-RM, S-RM) are simulated with a slit WG (width: λ_0/150). Two energy integration lines ($P_{\mathrm{out}} = P_{\mathrm{o1}} + P_{\mathrm{o2}}$) are placed 2$\lambda_0$ from the slit to avoid collecting the scattered waves from the slit. The energy tunneling efficiency is calculated as $\eta = P_{\mathrm{out}}/P_{\mathrm{in}}$. The electric field distributions at the eigenfrequency of slit waveguide for these cases are shown in Supplementary Fig.7c-e. So, in this case, the total length of the structure will not affect this transfer efficiency. Since only the surface mode energy is considered, radiation emitted by dipoles that do not couple to the surface wave is intentionally excluded. For the lossy grating (S-RM mode), the scattered light from the first two grooves is also excluded, explaining its lower efficiency in Fig. 2d.

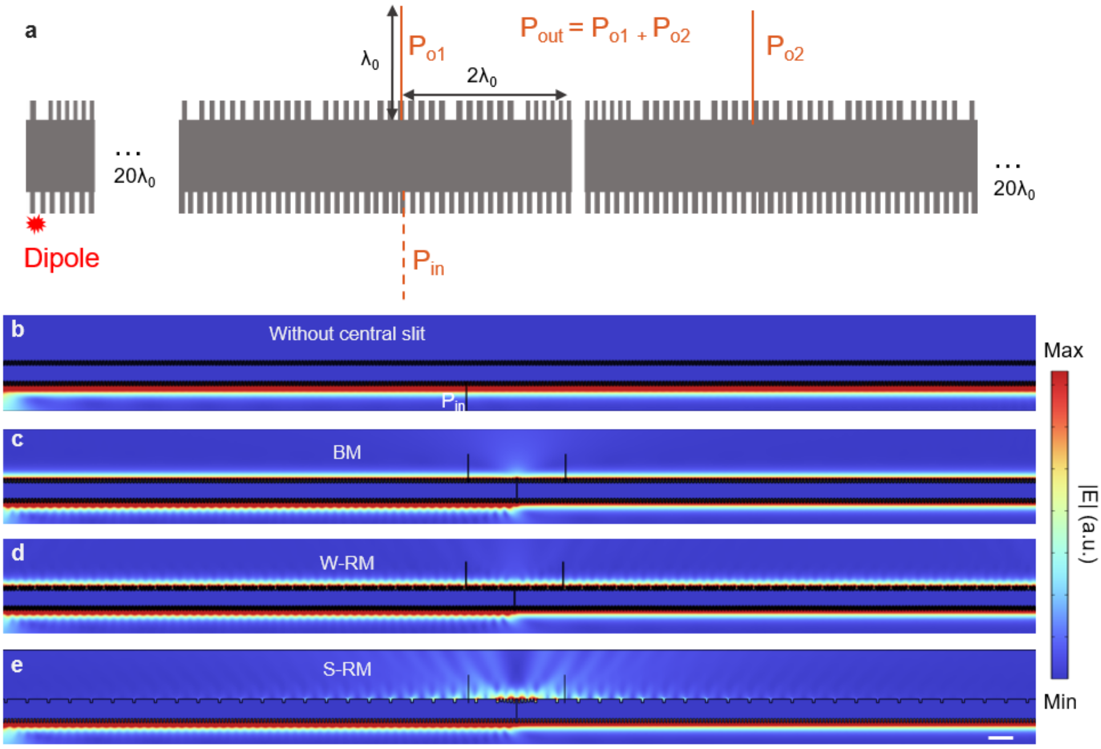

Supplementary Fig.7. Calculation of energy tunneling efficiency. a. Sketch of calculation method. A dipole source is placed at the edge of the bottom structure to excite the bottom surface mode. Two integration lines are set on the top surface near the center slit WG. The distance between the integration line and the slit is $2\lambda_0$. The orange dashed line is the integration line for the incident energy of the bottom surface mode. The slit is not constructed for the incident energy simulation. The length of the integration line is λ_0. The energy tunneling efficiency is calculated as: $\eta = P_{out} / P_{in}$. b. Electric field of the bottom surface mode at the eigenfrequency of slit WG. c-e. Electric field at the eigenfrequency of the slit WG for the whole structure with the structure of BM (bounded mode), W-RM, and S-RM (weak/strong radiation mode) on the top surface, respectively. The structure of BM is set as the bottom surface for all these simulations. Black lines on the bottom in b-d are the energy integration lines. Scale bar: λ_0.

Although our design shares structural similarities with those employed in extraordinary optical transmission (EOT) systems, it operates in the near field, in contrast to the far-field nature of EOT. Consequently, the efficiency metrics differ fundamentally due to the distinct excitation conditions involved. Classical EOT framework relies on surface waves excited by the grooves around the slit to enhance transmission. Because periodic boundary conditions are not suitable for the whole structure (a single slit with periodic grooves), the transmission of the entire device strongly depends on the simulation size. For this reason, most previous works have only reported relative enhancement compared to an isolated slit, rather than absolute transmission.

Nevertheless, approximate values can be inferred from reported results. For example, G. W. 't Hooft, et. al. reported their optimization could squeeze energy through the slit from around 20% of the width of the entire pattern (λ=800nm, groove number = 11)[18], implying an overall transmission efficiency of ~20% for the whole device. In our design, the simulated plane-wave transmission is ~14%, and the experimental value is ~10% (inset of Fig.3h), for a lateral size of ~20λ_0 (6 cm).

S 3.2 Efficiency optimization strategy

For the mode energy transfer efficiency (shown in Fig. 2d), although it is less than 10%, we also optimized the distance between the first groove and slit for both sides and designed the coupling region on the top side for mode S-RM, as presented in Supplementary Fig.5d. For the reason of the low efficiency and how to improve it, that's an open question, and we are happy to briefly discuss it with temporal coupled mode theory (TCMT)[15,19].

Case 1: The traditional giant transmission: plane wave input and plane wave output.

In this case, the system can be viewed as a two-port system, and the center slit functions as a resonant cavity, while the grooves on both surfaces function as a mode adapter between the plane wave and the slit mode, as shown in Supplementary Fig.7a.

The temporal dynamic evolution of the mode is described by the equation:

$$\frac{da(t)}{dt} = (i\omega_0 - \gamma_0 - \gamma_1 - \gamma_2)a(t) + \mathrm{K}^T|S_+\rangle, \tag{S19}$$

$$|s_-\rangle = C|s_+\rangle + \mathrm{D}a(t), \tag{S20}$$

where $a(t)$ is the complex modal amplitude as a function of time, ω_0 is the mode eigenfrequency, γ_0 is the nonradiative decay rate, γ_1, γ_2 are the radiative decay rates to the two ports, K = $[\kappa_1, \kappa_2]^T$ and D= $[d_1, d_2]^T$ are the coupling matrices between resonance and the two ports, $|s_+\rangle = [s_{1+}, s_{2+}]^T$ and $|s_-\rangle = [s_{1-}, s_{2-}]^T$ are the input and output waves.

Based on energy conservation, reciprocity, and time reversal invariance, we can derive the relationships between these coupling coefficients:

$$k_1 = d_1 = \sqrt{2\gamma_1},\ k_2 = d_2 = \sqrt{2\gamma_2}, \tag{S21}$$

$$C = \begin{bmatrix} -1 & 0 \\ 0 & -1 \end{bmatrix}. \tag{S22}$$

With time-harmonic input [exp($i\omega t$)], the solution of ER.1 can be written as:

$$a(t) = \frac{\mathrm{K}^T|S_+\rangle}{i(\omega-\omega_0)+\gamma_0+\gamma_1+\gamma_2}, \tag{S23}$$

When we assume the input as $|s_+\rangle = [1,0]^T$, the transmission coefficient can be expressed as:

$$t = \frac{s_{2-}}{s_{1+}} = \kappa_2 a(t) = \frac{2\sqrt{\gamma_1\gamma_2}}{i(\omega-\omega_0)+\gamma_0+\gamma_1+\gamma_2}, \tag{S24}$$

The transmission efficiency reaches a maximum under the following conditions:

a. Resonance condition: $\omega = \omega_0$;

b. No nonradiative loss: $\gamma_0 = 0$;

c. Critical coupling condition: $\gamma_1 = \gamma_2$.

Under these conditions, the transmission efficiency could reach $|t|^2$ = 100%.

The reason for the relatively low transmission efficiency in previous work at resonance frequency (~20% in paper[18]) came from the mode mismatch and metallic loss. The metallic loss is obvious in the optical band. Besides, the mode mismatch is the main reason for the limited efficiency. For the periodic groove grating with a single slit (bottom surface in Supplementary Fig.8b), the scattering field of the eigenmode is not an exact plane wave. Additionally, the eigenmode profile of the whole structure contains the surface wave at the edge of the structure (encircled in Supplementary Fig.8b), which makes the excitation efficiency degrade with only plane wave excitation. To verify the intrinsic limit, we excited the system with the reciprocal eigenmode profile at the focal plane and set the metal as a perfect electric conductor. Under this ideal matched excitation, the transmission reached 73.8%, demonstrating that >50% efficiency is achievable in principle (Supplementary Fig.8c). To further enhance the transmission to reach the theoretical maximum, coupling between the surface wave on both sides of the slit and the coupling between the surface wave and plane wave should also be further optimized.

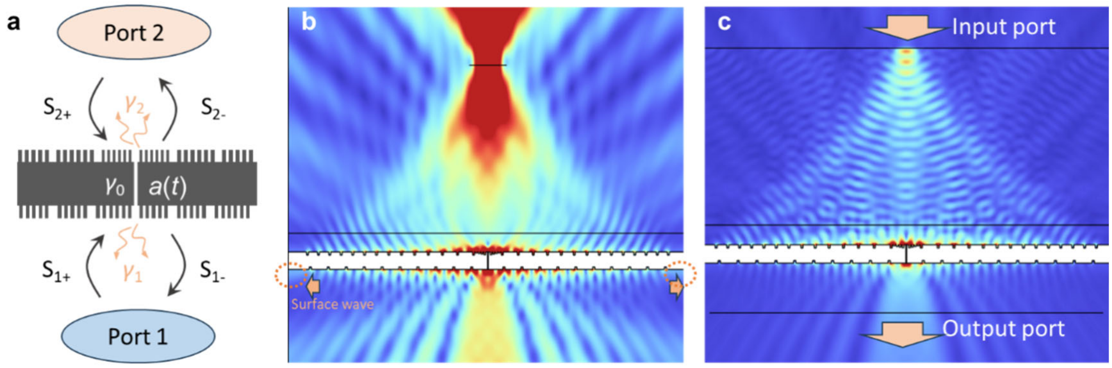

Supplementary Fig.8. Transmission efficiency analysis. a. Sketch of the design coupled with two free-space ports. b. The |E| field of the eigenmode of the design. The dotted circle and the orange arrow indicate the surface wave at the edge of the structure. c. The |**E**| field profile of the design excited with the reciprocal field of the eigenmode at the focal plane. Input and output ports are marked in the figure.

Case 2: Surface wave input and output (energy transmission efficiency in our paper).

Due to the incoherent nature of thermal excitations, the global eigenmode of the bottom surface cannot be coherently excited by incoherent thermal dipoles at different positions. In this case, the bottom surface is treated as a waveguide for the thermally excited surface waves.

Similar to the energy calculation in Supplementary Fig.5, we further monitored the energy transporting efficiency at different ports (Port 1-6, P1-P6) as indicated in Supplementary Fig.9a. We found that most of the energy (75%) is reflected in P1 and only ~13% energy is transported to the top side. This low efficiency is fundamentally caused by the large momentum mismatch between the bottom surface wave (primarily k_x component) and the slit waveguide mode (k_z component). Since the slit and surface waveguide are orthogonal, this mismatch is difficult to eliminate, and groove–slit spacing provides limited tuning freedom, which was also applied in the optimization of the structure.

If device footprint constraints are relaxed, this energy efficiency can be greatly boosted by designing the bottom surface as a cavity. When we apply an additional constraint on the surface mode, such as adding a metal board above the grooves with a specific gap, the surface wave mode transforms into a different guided mode with a specific bandgap, as shown in Supplementary Fig.9b. The bottom surface cavity can be formed by introducing a defect in the photonic crystal. In this case, Bragg reflection of the photonic crystal could further confine the thermal energy distribution around the slit and enhance the energy efficiency. We applied a similar simulation method shown in Supplementary Fig.9c, the system can reach 75% absorptivity (reciprocally emissivity) at eigenfrequency by applying suitable absorption in the bottom photonic crystal defect cavity. However, the photon collection area is limited by the effective mode area in this case.

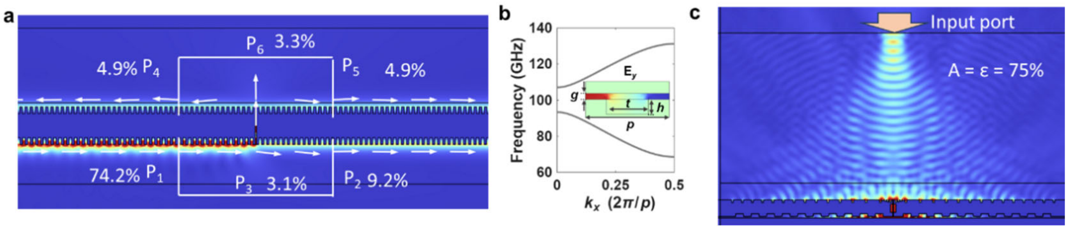

Supplementary Fig.9 Transmission analysis for the incoherent thermal source. a. Energy transportation occurs at each port. P_1-P_6 are the incident port, direct transmit port, backscattering port, transmit port for the left side, transmit port for the right side, and the free-space scattering port, respectively. The arrows indicate the Poynting vector. The energy received by each port is marked in the figure. b. Band-diagram of the photonic crystal unit cell. Inset shows the E*y* field of the eigenmode profile. *t*, *h*, *p*, and *g* are 1.4 mm, 0.5 mm, 2.8 mm, and 0.2 mm, respectively. c. The |**E**| field profile of the design excited with the reciprocal field of the eigenmode at the focal plane. Input port and absorptivity A (reciprocally, emissivity ε) are marked in the figure.

Increasing the number of funnels per wavelength is certainly an intuitive approach to boosting the emission power. However, the key challenge lies in ensuring coherent resonance among the funnels. If the funnels resonate in an uncorrelated manner, the resulting emission is merely an intensity superposition of the individual emission profiles, which increases the total power but does not yield constructive interference or a more refined emission pattern. Achieving phase correlation across the funnel array requires an additional bottom surface-mode cavity, which could enhance the power while also enlarging the spatial coherence on the top surface. This is a promising direction that warrants further exploration in future work.

S.4 Design and optimization of grooves for self-focusing meta-emitter

To better harvest the surrounding heat, S-RM is applied to the bottom side of the device. For the grooves on the top side, W-RM is applied and the position of local scatters is designed by the holographic approach, as Supplementary Fig.10a schematically shown. Specifically, the scatter position is determined based on the interference pattern of the diverging spoof surface plasmon polaritons (spoof SPPs, as the reference beam) on the surface from the waveguide (WG) and diverging wave originating from the focal spot in free space (signal waves)[20,21]. For simplicity, we ignore the amplitude decay of spoof SPPs along the surface. The phase profile can be expressed as:

$$\begin{cases} \varphi(x) = k_0 \cdot \left(\sqrt{x^2 + f^2} - f\right), \\ \varphi(x) + k_{\mathrm{sspp}} x = 2m\pi, \end{cases} \tag{S25}$$

where x is the coordinate on the surface, f is the focal length, k_0 is the free-space wavevector, m is an integer, and k_{sspp} is the wavevector of the spoof SPPs. We set f = 3 cm, $k_0 = 2\pi/\lambda_0$, where λ_0 = 3 mm is the target wavelength. k_{sspp} / k_0 initially set to 1.01. Owing to the non-uniform spacing among different scatterers on the top surface, the quantity and periodicity of the nonlocal grooves situated between scatterers are meticulously adjusted to evenly span the available spacing. To offset the wavevector discrepancies arising from the periodic differences of these nonlocal grooves, the depth of the grooves is concurrently adjusted, ensuring a consistent wavevector distribution across the entire surface. The period and depth of these nonlocal grooves can be concisely expressed as:

$$\begin{cases} p = \Delta x / \mathrm{round}\left(\frac{\Delta x}{p_4}\right), \\ N = \mathrm{round}\left(\frac{\Delta x}{p}\right) - 1, \\ h = h_4 + dh_4 * \left(\frac{p}{p_4}\right), \end{cases} \tag{S26}$$

wherein Δx is the spacing between neighboring scatters, p_4, h_4 and dh_4 are respectively the initial period, depth and depth difference of these nonlocal grooves, p, N, and h are respectively the adjusted period, number and depth of these grooves. Then, the original design of the 1D self-focusing emission is developed, and its focusing performance is simulated in COMSOL Multiphysics.

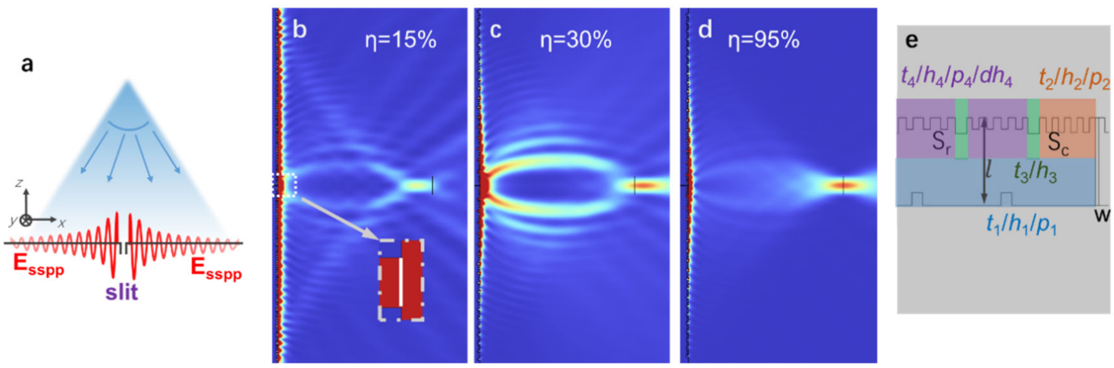

Supplementary Fig.10. The design and optimization of the top meta-emitter. a. Schematic diagram of local scatters designed by holographic approach. The scatter position is determined based on the interference pattern of the diverging spoof SPPs (the reference beam) on the surface from the WG and diverging wave originating from the focal spot in free space (signal waves)[20,21]. b-d. The focusing performances of surface structure without optimization or coupling region, with optimization but without coupling region and with both optimization and coupling region, respectively. The focal efficiencies, defined as the ratio of integrated energy at the focal line (marked by the black lines) to the output energy at the exit of the WG (marked by the white lines drawn in the inset in a), are provided in the corresponding figures. e. Structure and parameters in 1D self-focusing meta-emitter. The variables t_i, h_i and p_i denote respectively the width, depth, and period of the groove structures, with i = 1, 2, 3 and 4 representing the region of the bottom surface (blue zone), the coupling region (S_c, orange region), the radiative surface (S_r, green region), and between the local scatters (S_r, purple region), respectively. The variables l and w denote respectively the length and width of the WG.

The focusing performance of the initial trial is presented in Supplementary Fig.10b, which exhibits poor surface wave modulation. The focusing efficiency η of the device is defined as the ratio of the integrated energy at the focal line (indicated by the short black line in Supplementary Fig.10b) to the energy at the WG exit (depicted by the white solid line in the inset of Supplementary Fig.10b). The focusing efficiency of the initial trial is 15%. A built-in optimization algorithm of Nelder-Mead is applied to adjust the wavevector of spoof SPPs (k_{sspp}), and the size of grooves in the radiative surface (denoted as S_r in Fig. 3a in the main text) to maximize the focusing efficiency. The optimized η reaches 30%, as drawn in Supplementary Fig.3c, but more than half of the energy is scattered as background noise. To further improve η, a coupling surface S_c is introduced to compensate for the transverse momentum mismatch between WG mode and spoof SPPs[22]. The optimized η for the design with S_c reaches 95%, as shown in Supplementary Fig.10d. The structural parameters of the grooves are schematically given in Supplementary Fig.10e, with specific values provided in Supplementary Table 2.

The ensemble averaged results shown in Fig. 3e-f are obtained in the Ansys Lumerical FDTD Solutions for the 3D simulation of the entire design. An electric dipole with a random phase, orientation angle, and x, y coordinates is placed on the bottom surface

($0.3\lambda_0$ away from the bottom surface) as the source to capture the intensity profiles at different frequencies for each plane. This simulation is repeated 100 times, each with a different random dipole source. The average of all simulated intensity profiles is then calculated to obtain the statistical emission profiles for each plane, as shown in Fig. 3e-g. In the simulations, the emission intensities of all random dipoles are set identically. The transmitted energy obtained from each dipole simulation is shown in Supplementary Fig.11 , where the differences originate from the varying coupling efficiencies between individual random dipoles and the bottom surface mode. This excitation-efficiency variation reflects the fundamental process by which thermally populated surface waves are generated, namely that dipoles with near-normal surface polarization possess higher excitation efficiency. Such coupling-induced transmittance fluctuations do not affect the coherence enhancement performance of the designed resonant tunnel.

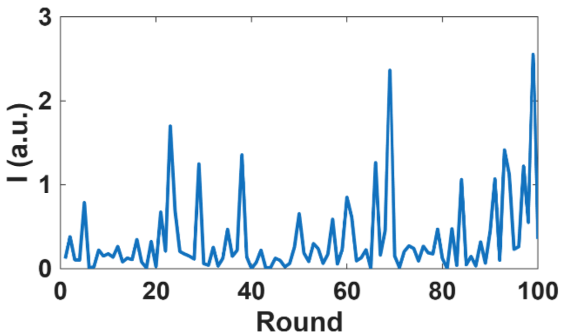

Supplementary Fig.11. Transmittance fluctuation in 100 random dipole excitations

S.5 Time-domain analysis for the emission behavior of self-focusing meta-emitter

All the designs in Supplementary Note S4 are based on the frequency-domain simulation in COMSOL Multiphysics, where the device is excited by the coherent source at the target wavelength. When it comes to thermal radiation, the generated pattern of the device can be treated as the statistical average of contributions from all the stochastic emission processes on the bottom surface over time. It can be expressed by the ensemble average[23]:

$$\langle x(t)\rangle_e = \lim_{N\to\infty}\frac{1}{N}\sum_{k=1}^{N} {}^{k}x(t), \tag{S27}$$

and the time average:

$$\langle {}^k x(t)\rangle_t = \lim_{T\to\infty}\frac{1}{2T}\int_{-T}^{T} {}^k x(t)\mathrm{d}t, \tag{S28}$$

taken over all the processes on the bottom, where ${}^k x(t)$ is a typical realization of the process. Since the WG supports only a single mode within the designed frequency band, all energy from the bottom-side emission processes will first couple to this WG mode before reaching the top side. As a result, variations in the bottom-side contributions manifest solely as changes in the intensity of the top-side emission properties. This allows the wavefront performance on the top side to be inferred from a single bottom-side emission process. Furthermore, as a statistically stationary process, ergodicity ensures that the time average and ensemble average yield identical results. Therefore, the time-averaged behavior of any single bottom-side emission process can accurately represent the overall emitting behavior on the top side.

Thus, we conduct a time-domain simulation in COMSOL Multiphysics to analyze the resonance and emission behavior of the device. A randomly distributed line current source along the *y* direction is applied. The time-dependent electric field of source is expressed as:

$$E(t) = \sin(\omega_0 t)\exp\left(-\frac{(t-t_0)^2}{dt^2}\right), \tag{S29}$$

where $\omega_0 = 2\pi * 100\ \mathrm{GHz}$ is the angular frequency, t_0 = 25 ps is the offset of the electric field oscillation, and *dt* = 10 ps is the pulse length, which equals the time it takes for light to propagate over one central wavelength. According to the Wiener-Khinchin theorem[23], the spectrum density of a wide-sense-stationary random process can be obtained by the Fourier transform of its auto-correlation function. Figure S10a presents the time-dependent electric field of the source, along with its spectrum density in both wavelength and frequency domains.

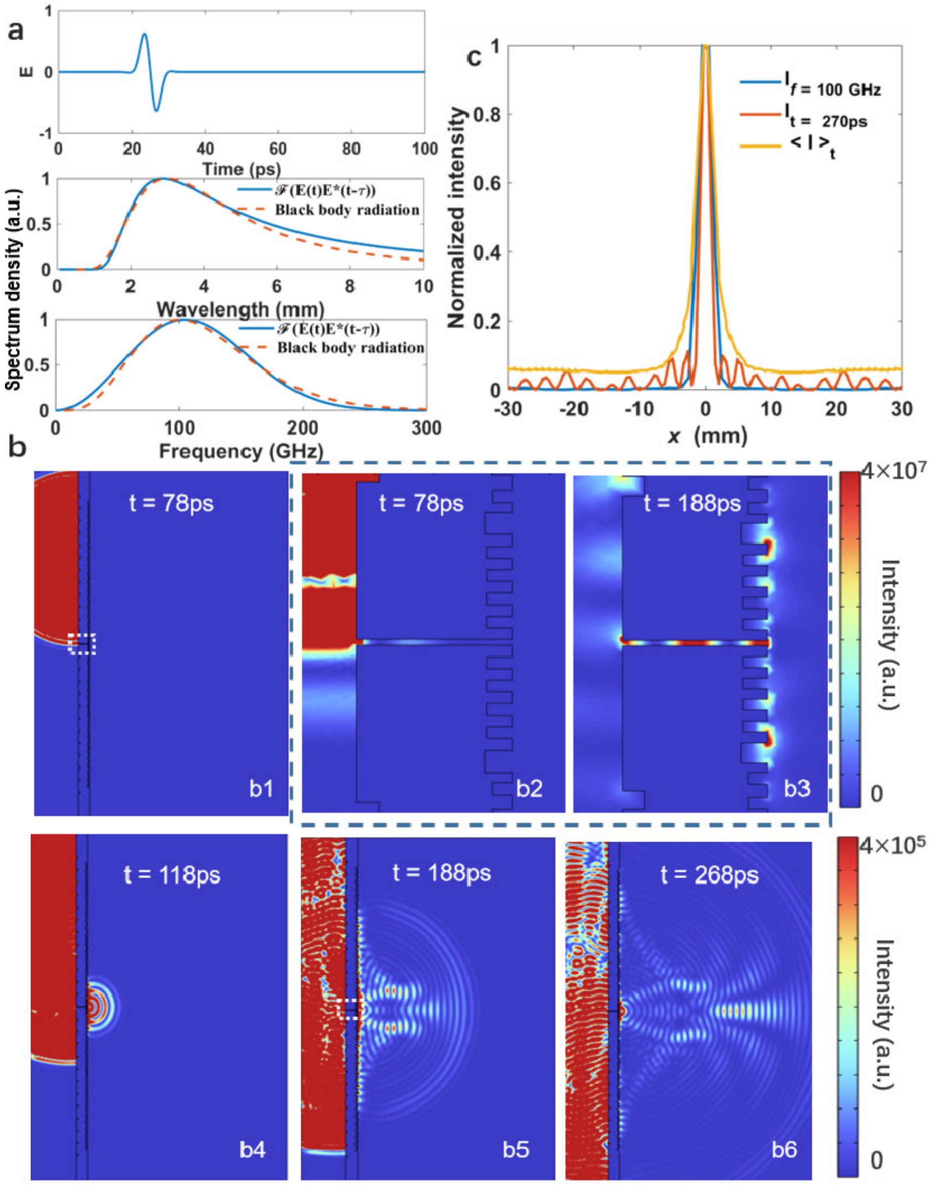

Supplementary Fig.12. Time domain simulation of the design. a. The time-dependent electric field of the line source and its Fourier transform in wavelength and frequency domain. b. Intensity profiles of the design under line source excitation at different times. Subfigures b2 and b3 are the enlarged dashed regions in b1 and b5, respectively, to clearly show the intensity distribution in the WG. Subfigures b1- b3 share the same color bar at the top, while b4-b6 share the color bar at the bottom. c. The intensity distributions at the focal plane for t = 270 ps, time average, and the eigenmode in Fig. 3b.

A dynamic time-dependent electric field for the entire device can be obtained, as shown in Supplementary Movie 1. The dynamic interactions between spoof SPPs and the WG mode, as well as the photon lifetime enhancement effect caused by the WG mode, and how the focal line is formed, are clearly observed in the movie. Several time-slice intensity profiles are drawn in Supplementary Fig.12b. At t = 78 ps, the wave package reaches the WG. Then it excites the WG mode and is scattered out in a cylindrical diverging wave at the exit of the WG at t = 118 ps. At t = 188 ps, a clear WG mode pattern can be observed and the scattered field at each top groove constructively interferes, forming the focal wavefront. At t = 268 ps, a clear focal line is formed at the designed position. By taking the time average of all the electric fields (S4), the thermal emission behavior at the focal plane can be achieved, as shown in Supplementary Fig.12c. For better comparison, the intensity distribution of the eigenmode (presented in Fig. 3b) and the time-slice at t = 270 ps at the focal plane are also plotted in Supplementary Fig.12c. The focusing behavior of the thermal emission aligns well with the eigenmode, with only minor background noises introduced, which is caused by the non-static state of the WG mode at the beginning of the emission.

S.6 Out-of-plane wavevector dispersion feature of the WG mode

S.6.1 Derivation of the out-of-plane wavevector dispersion

The Fabry-Pérot (FP) resonance-based WG mode allows all the EM wave with combinations of the wavevectors and frequencies that satisfy the condition of $k_z \cdot l = m\pi$ to transmit, where k_z is the wavevector at the z direction and l is the WG length. For a given FP mode (with fixed m and l), the WG acts as a filter, transmitting only waves with a constant k_z. Additionally, since the WG mode exhibits no phase variation along the x-direction (k_x = 0), transverse wavevector k_y and wavevector along the WG k_z can be expressed as:

$$\begin{cases} k_y = k_0 \cdot \sin\theta \\ k_z = k_0 \cdot \cos\theta \end{cases}, \tag{S30}$$

where θ can be viewed as the angle between the k_y and z axis and k_0 is the vacuum wavevector.

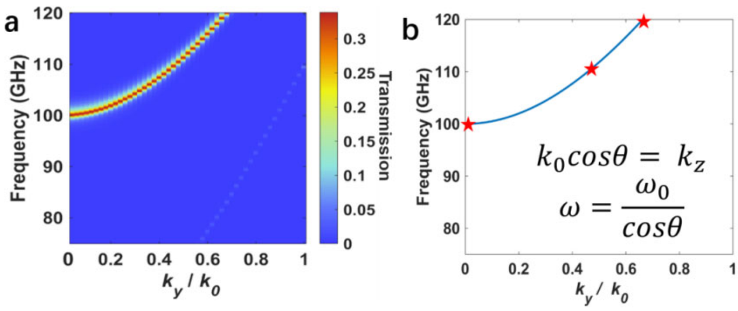

Supplementary Fig.13. Out-of-plane dispersion of the WG mode. a. Simulation result. b. calculated result, which is the same as that in Fig. 3c in the main text. The star marks denote the k_y and corresponding frequencies in Supplementary Fig.14b-d.

When we design the WG mode at an angular frequency of ω_0 = 2π·100 GHz at k_y = 0 (θ = 0, without out-of-plane wavevector), constant k_z at different frequencies ensures the equation of

$$\omega/c^*\cos\theta = \omega_0/c, \tag{S31}$$

where c is the light speed. The k_y dispersion can be derived by substituting the θ expression in Eq. S30 into S31. The resulting dispersion relation is shown in Supplementary Fig.13b, which has good agreement with the simulated result in Supplementary Fig.13a .

S.6.2 Dipole excitation simulation.

This dispersion feature can also be observed in the simulation. A full 3D simulation is conducted using Ansys Lumerical FDTD solutions. A randomly distributed dipole is positioned at the bottom surface (at x = 13.6 mm, y = 11.5 mm, z = -3.5 mm) as the source. The intensity profiles of responses at yz (center plane of the device) and xy (top surface of the device) planes at different frequencies are drawn in Supplementary Fig.14. The projection of the dipole position on each plane is marked with a red star in the figures.

At 90 GHz, the WG mode cannot be excited, leading to a weak scattering field on the top side of the WG, as illustrated in Supplementary Fig.14a and e. At the designed frequency of 99 GHz, the WG mode is efficiently excited at the y-position corresponding to the dipole's y-coordinate, as shown in Supplementary Fig.14b and f. At higher frequencies (109 GHz and 119 GHz), the WG pattern emerges at different positions along the WG, as demonstrated in Supplementary Fig.14c-d and g-h. The excitation frequencies and their corresponding transverse wavevectors k_y (calculated based on the center of the WG pattern and the dipole position) are indicated in Supplementary Fig.13, exhibiting excellent agreement with the predicted dispersion curve.

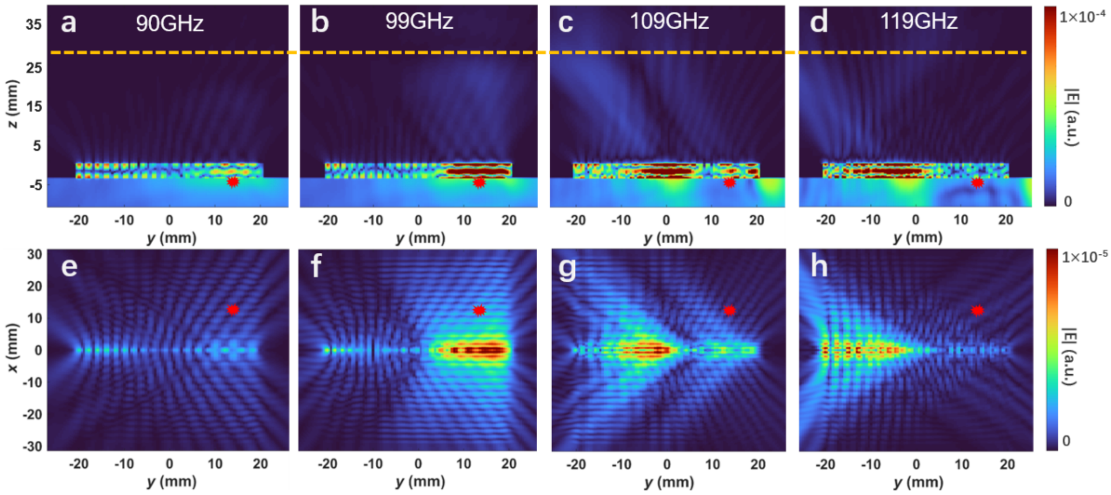

Supplementary Fig.14. Simulation of the |E| field profile under the dipole excitation. a-d. The electric field profiles at x = 0 plane under 90, 99, 109, and 119 GHz, respectively. The yellow dashed line indicates the focal plane. e-h. The electric field profiles at the z = 0 plane under 90, 99, 109, and 119 GHz, respectively. The dipole position is at x = 13.6 mm, y = 11.5 mm, z = -3.5 mm. The condition (k_y, ω) of subfigures b-d is indicated with star marks in Supplementary Fig.13. The red mark in each figure denotes the position projection of the dipole on each plane.

At the exit of the WG, the FP mode efficiently transforms into the spoof SPPs, corresponding to the k_z components of FP mode entirely converting into the k_x components of the spoof SPPs. Consequently, the fixed k_z of the WG mode results in a uniform k_x for the spoof SPPs on the top surface, ensuring that the focal length in the xz-plane remains the same along the dispersion curve. In Supplementary Fig.14, the focal plane position is marked by the yellow dashed line, which aligns with the maximum intensity lines in the yz-plane, further confirming the achromatic property of the WG mode for out-of-plane wavevectors. A large k_y only tilts the focusing profile, creating an oblique focus along y-direction, while the projection distance in the xz-plane remains unchanged.

S.7 Analysis of lifetime and decay length degradation of surface modes caused by weak absorptive layer

The blackbody paint used in our experiment (Musou Black 2.0) is highly absorptive in the visible and infrared bands but only weakly absorbing in the millimeter-wave regime. We measured the reflectivity of a ~500 μm BB layer coated on a copper plate using a vector network analyzer (VNA). The layer thickness was determined by measuring the height difference between the bare and the coated metal surfaces with a micrometer. As shown in Supplementary Fig. 15a (measurement setup in the upper inset), the reflectivity decreases only slightly to ~96% compared with the bare copper surface. To characterize the absorption of this material, we simulated a 500 μm BB layer on metal. By setting the extinction coefficient (imaginary part of the refractive index) to 0.02, the simulated reflectivity also reduces to ~96%. The corresponding loss density distribution is shown in the inset of Supplementary Fig.15a. These results confirm that the BB layer behaves as a weak absorber at millimeter-wave frequencies.

We further repeated the lifetime and decay-length simulations for the three surface modes discussed in the main text, now including a ~60 μm BB layer (the same thickness used in the experiment). The results are presented in Supplementary Fig.15b, with the corresponding loss distributions in Supplementary Fig.15c. The additional absorption substantially reduces the lifetime and decay length of the BM and W-RM modes by approximately two and one orders of magnitude, respectively, compared with those shown in Fig. 2g. Because the S-RM mode features weak localization, this additional loss has only a minor effect—its lifetime and decay length decrease by only ~10% relative to the lossless case. Considering the size of our device, only the S-RM mode is used in the experiment, and the BB layer therefore has a negligible impact. For larger devices, however, such absorption would indeed reduce the effective collection area.

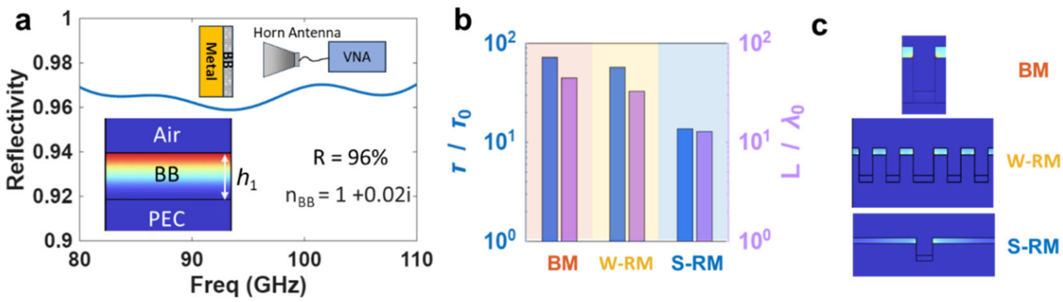

Supplementary Fig.15 Degradation of surface-mode lifetime and decay length due

to the BB layer. a. Reflectivity of the BB-coated metal surface. The upper inset shows the measurement setup. Left bottom panel presents the loss density distribution. The extinction coefficient of BB is 0.02 in the simulation. b. Lifetime and decay length of the three discussed modes with ~60 μm BB coating. c. Loss distribution for the three discussed modes.

S.8 Fabrication tolerance analysis

S 8.1 Impact of geometric fabrication errors.

Deviations in groove width, depth, and position lead to variations in the radiative phase of surface-wave emission, which degrade the overall wavefront modulation performance. Due to the narrow width of the designed scatterers (around $\lambda_0/10$), the emitted phase can be simplified to solely depend on the propagation phase ($\varphi = k_{\mathrm{sspp}}x$) of the spoof SPPs. Errors in groove width and depth mainly cause the wavevector (k_{sspp}) deviation, and the groove position (x) errors directly cause the propagation phase deviation. We conducted the simulation of wavevector deviation (δk) on groove width and depth deviation (δw and δh) in one unit cell, as presented in Supplementary Fig.16a-b. Around 1% fabrication error in width and depth causes 1.5% and 6% of wavevector deviation (δk). Positional deviation (δx) approximately proportional to the scattered phase deviation ($\delta\varphi$), as plotted in Supplementary Fig.16c.

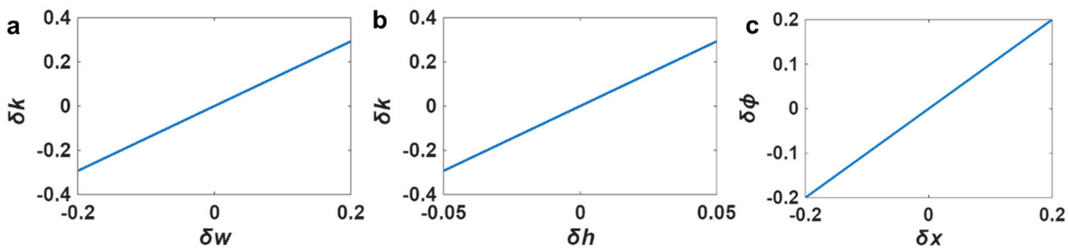

Supplementary Fig.16 Fabrication tolerance analysis. a-b. Surface wavevector deviation as a function of groove width and depth variation. c. Scattered phase deviation as a function of groove position deviation.

S 8.2 Tolerance criterion based on optical wavefront aberration.

In traditional optical systems, wavefront deviation (wavefront aberration) less than $1/4\lambda_0$ are generally considered acceptable. Borrowing this criterion, the allowable fabrication tolerances for our wavefront-modulation device are approximately: groove width, depth, and position tolerance are about ±17%, ±4% and ±25%.

S 8.3 Compatibility with CNC fabrication precision.

State-of-the-art CNC machining can achieve groove-width, groove-depth, and position accuracies of approximately ±0.02 mm, ±0.01 mm, and ±0.004 mm, respectively, corresponding to fabrication errors of ~±10%, ±9%, and <±0.5%. These values fall within the individual tolerance limits noted above.

However, the accumulated phase error can become significant if all parameters deviate simultaneously near their upper tolerance limits. In such a worst-case scenario, the combined phase error can approach ~20%, close to the allowable tolerance boundary. This accumulated phase deviation accounts for the observed higher-order diffraction in the holography patterns and local minima near the slit in the self-focusing thermal emission.

S 8.4 Analysis of local minima intensity around the WG exit in the experiment

The observed intensity local minima near the center slit originates from the non-ideal interference of the waves scattered from the left and right sides of lens grooves, due to the depth fabrication error in the coupling region around the slit exit. We conducted the simulation of the structure with 10% larger groove depth, the scattered phase from the first groove on the both side of the device could form a destructive interference in the near-field as Supplementary Fig.17b shown. Supplementary Fig.17a (same as Fig. 3e) is the ideal scattering case, these two groove are constructive interference at center. The measured intensity profile in Supplementary Fig.17c is the more like the combination of the both cases, but the interference minima is more obvious at the near-field. This fabrication error only has large influence on the near-field intensity distribution, and would obviously affect the far-field pattern, as we measured in the experiment.

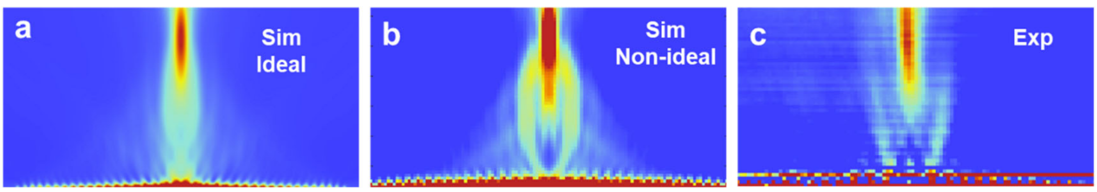

Supplementary Fig.17 Constructive and destructive interference cases around the slit exit. a-b. Simulation results for the ideal structural parameters and non-ideal structural parameters with 10% deeper groove depth of the coupling region (S_c in the Fig. 3a in the Main Text). c. Measured result.

S.9 Feasibility of point-by-point intensity mapping measurement

The thermal radiation pattern of the sample is measured point-by-point using a detector mounted on a translation stage. To improve the accuracy of the mapping measurement, a WG probe with a sharp tip is designed for the detector. The detection performance is evaluated through simulations in COMSOL Multiphysics. As illustrated in Supplementary Fig.18a, a metal probe with sharp tips is modeled, and the collected energy is integrated at the probe's end. By scanning the probe, the spatial intensity profile is obtained, as shown in Supplementary Fig.18b. This profile closely aligns with the ground truth intensity distribution, confirming the accuracy of our mapping measurement. A photograph of the fabricated probe antenna is provided in the inset of Supplementary Fig.19a. The pictures of the experimental setup from different views are shown in Supplementary Fig.19a-b. For better comparison, the cross-sections of the intensity profiles in simulation and experiment at each plane (Fig. 3 in the main text) are plotted in Supplementary Fig.19c-e. Measured results align well with simulations in all these cross-sections.

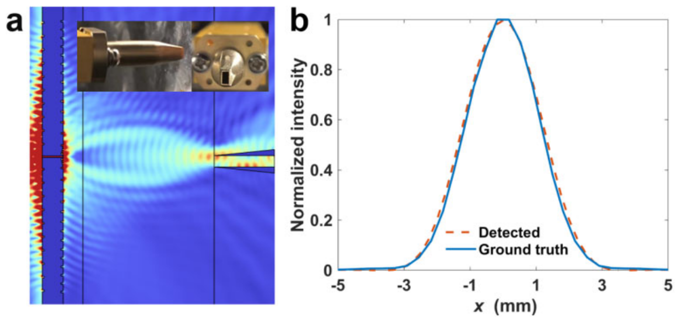

Supplementary Fig.18. Detection performance of the probe antenna. a. The intensity profiles with a sharp-tip probe antenna at y = 1 mm. The inset is the picture of the antenna applied in the experiment. b. The variation of the energy received by the antenna with the antenna's position compared with the ground truth. The received energy is obtained by integrating the Poynting vector at the end of the antenna.

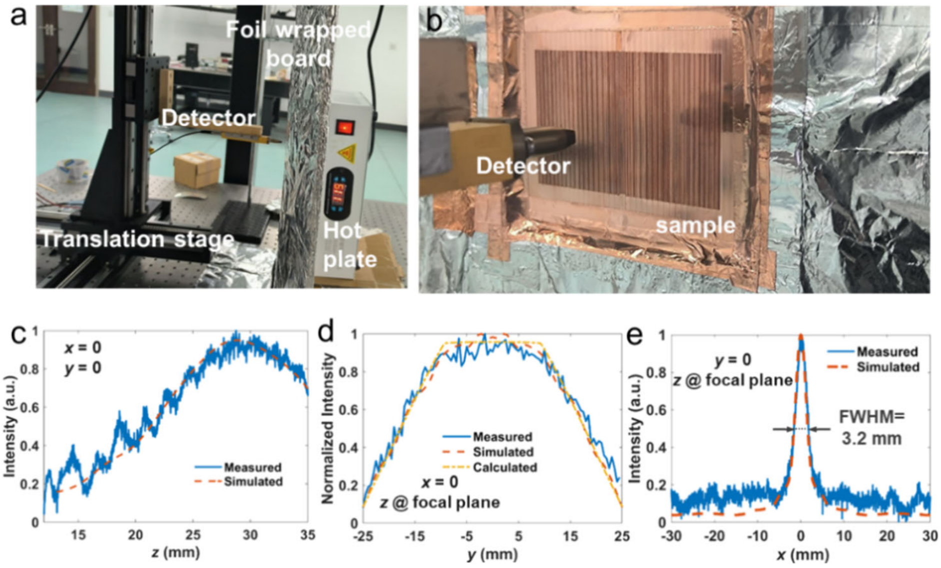

Supplementary Fig.19. Detailed experimental information. a-b. The experimental setup. c-e. The cross-sections of the intensity profile in simulation and experiment at different planes.

S.10 Calculation of the focal line shape

In this section, we use a ray tracing approach to analyze the contribution of each dipole at the bottom surface to the intensity profile of the focal line.

From Supplementary Note S4, we know that the cylindrical surface wave package emitted by a dipole source could excite the WG mode at different frequencies with different out-of-plane wavevectors. In other words, each part of the cylindrical surface wave package emitted from a dipole source can transmit through the WG at the corresponding frequencies. For simplicity, we assume the coupling efficiencies for waves with any k_y to the WG mode are equal. For a single emission process originating from point D(x_0, y_0, -l), as schematically drawn in Supplementary Fig.20a, the electric field intensity at any position at center WG, P(0, y_1, -l) is only determined by the propagation decay along the surface:

$$I_{D\to P} \propto \exp\left(-\alpha \cdot |DP|\right) \tag{S32}$$

where α is the decay rate of the spoof SPPs on the bottom surface.

The light ray DP points to the point Q(0, y, f) at the focal plane, which can be expressed as:

$$y = y_1 + \tan(\theta) \cdot (f + l) \tag{S33}$$

where f and l are respectively the focal length and WG height, and θ is the angle between DP and the unit vector along the *x*-axis, as shown in Supplementary Fig.20a. For our 1D focusing device, an electromagnetic (EM) wave originating from any arbitrary point P at the waveguide (WG) exit refocuses to the predefined focal point Q, with energy conservation maintained between these two spatial coordinates during a single emission cycle.:

$$I_Q(y) = I_P(y_1, \theta) \tag{S34}$$

Equations S32-34 predict the intensity and position of the focal spot Q emitted by the dipole source at D and traveled from the P point on the WG. By integrating the contribution of all the dipoles on the bottom surface and all the points P at the finite size of the WG, the intensity distribution along the focal line is obtained:

$$\begin{cases} I_P(y_1, \theta) \propto \iint \exp\left(-\alpha * \sqrt{x_0^2 + (y_0 - y_1)^2}\right) dx_0 dy_0, \\ \tan\theta = \frac{(y_0 - y_1)}{x_0}, \\ I_Q(y) = \int I_P(y_1, \theta) \mathrm{d}\theta \end{cases} \tag{S35}$$

Considering the finite frequency response range of our detector, EM waves with a frequency higher than the cut-off frequency of the detector can’t be measured, which affects the shape of the focal line in the realistic measurement. Since the resonance frequency of the WG mode depends on the angle θ (related to the transverse wavevector k_y), the band-limiting effect can be incorporated into the integration limit in Eq. S35 as:

$$I_Q(y) = \int_{-\theta_1}^{\theta_1} I_P(y_1, \theta) \mathrm{d}\theta \tag{S36}$$

where θ_1 can be derived from the corresponding k_y of the detector’s cut-off frequency. The frequency response of our detector, plotted in Supplementary Fig.20b, is effective only within the band of 75-120 GHz. The intensity distributions of the focal lines with different integration bands are plotted in Supplementary Fig.20c. The limited response range leads to a flat-top intensity distribution along the focal line. As the integration range is extended, this flat-top behavior gradually smooths out. When contributions from all frequency components are considered, the intensity distribution of the focal line transitions into a near Lambertian emission curve, as illustrated in Supplementary Fig.20c.

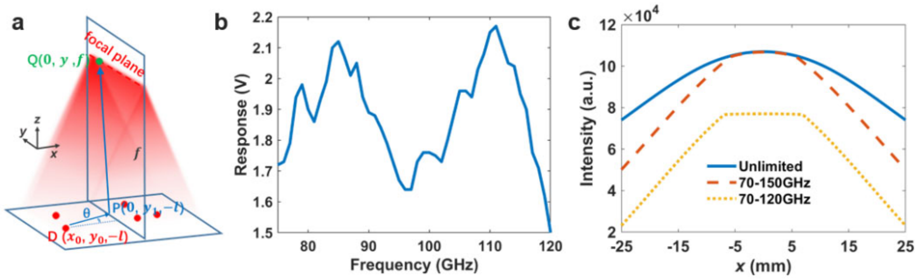

Supplementary Fig.20. The sketch of the calculation of flat-top behavior caused by the limited responding range. a. The configuration of the intensity calculation of the focal line. b. The frequency response behavior of our detector. c. The calculated intensity distribution along the focal lines with different integration bands.

S.11 Design method and detailed emission performance of the polarization multiplexed sample

Similar to the holographic design approach proposed in Supplementary Note S2, the groove position is also obtained by the interference pattern of the diverging spoof SPPs and the objective wavefront. However, the amplitude decay of spoof SPPs along the surface is considered here:

$$E_{\mathrm{sspp}}(x) = A_0 \exp(-\alpha x) \exp(ik_{\mathrm{sspp}} \cdot x), \tag{S37}$$

where α is the spatial decay rate determined by the scattering loss of the spoof SPPs, k_{sspp}, and x is the wavevector of spoof SPPs and the coordinate on the surface.

To counteract the inherent attenuation of spoof surface plasmon polaritons (SPPs) during holographic recording, we introduce an artificially amplified spoof SPPs field with controlled amplitude modulation:

$$E_{\mathrm{a,sspp}}(x) = A_1 \exp(\alpha x) \exp(ik_{\mathrm{sspp}} \cdot x + \varphi), \tag{S38}$$

where φ is a bias phase for further optimization.

For the objective wavefronts for different functions, they are designed as:

$$E_{\mathrm{o}}(x) = \begin{cases} A_2 \exp\left(ik_0 \cdot \left(\sqrt{(x-x_0)^2+f^2}-f\right)\right), \quad \text{for single offaxis focusing} \\ A_2[\exp\left(ik_0 \cdot \left(\sqrt{(x-x_0)^2+f^2}-f\right)\right) + \exp\left(ik_0 \cdot \left(\sqrt{(x+x_0)^2+f^2}-f\right)\right), \\ \qquad \text{for the double offaxis focusing} \\ A_2[\exp\left(ik_0 \cdot \left(\sqrt{(x-x_0)^2+f^2}-f\right)\right) + \exp\left(ik_0 \cdot \left(\sqrt{x^2+f^2}-f\right)\right) + \psi) \\ \quad + \exp\left(ik_0 \cdot \left(\sqrt{(x+x_0)^2+f^2}-f\right)\right), \quad \text{for triple focusing} \end{cases} \tag{S39}$$

where x_0 is the offset of the focus, k_0 is the free-space wavevector, f (=20 mm) is the focal length and ψ is the phase bias in the triple focusing design.

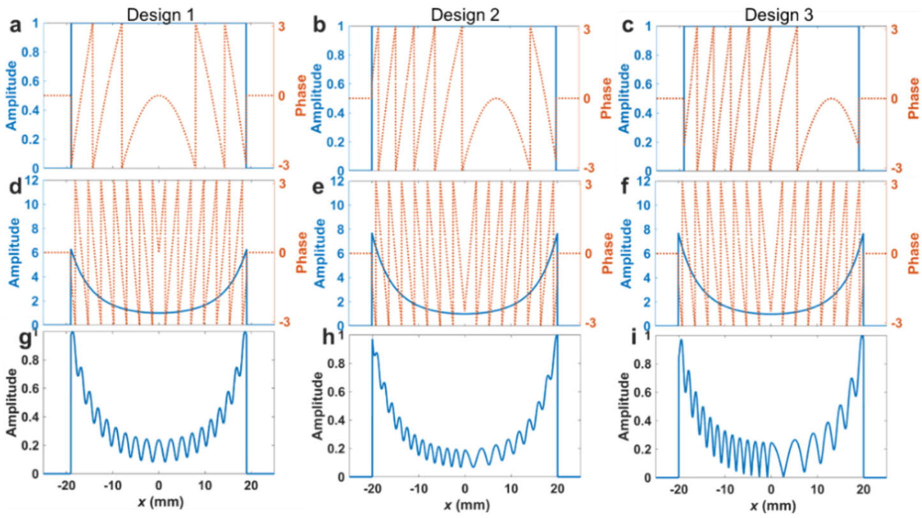

Supplementary Fig.21. Design of the single focusing device. a-c. Amplitude and phase distribution for designs 1-3. d-f. The amplitude and phase of the diverging spoof SPPs for design 1-3. g-i. The interference pattern of the spoof SPPs and signal waves for designs 1-3.

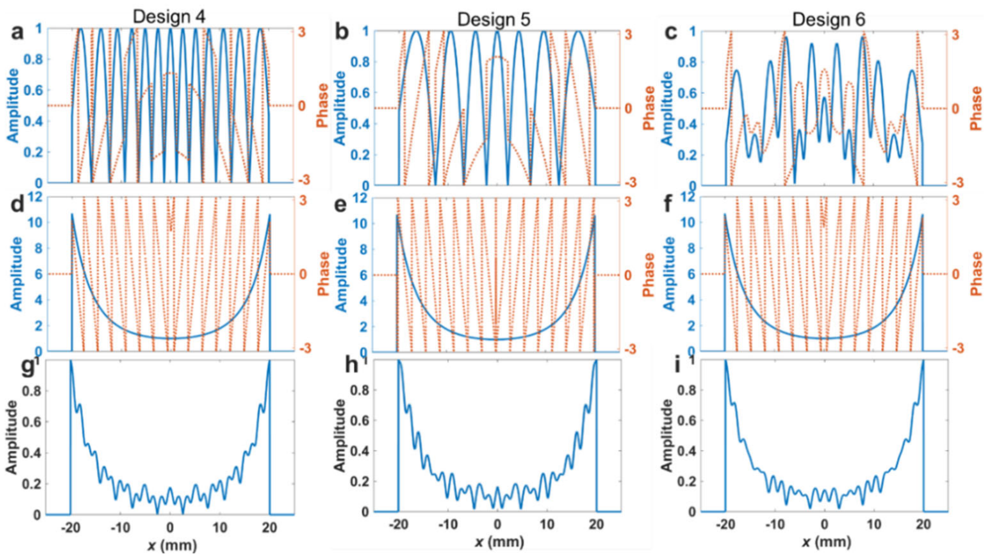

Supplementary Fig.22. Design of the multiple focusing device. a-c. Amplitude and phase distribution for design 4-6. d-f. The amplitude and phase of the diverging spoof SPPs for design 4-6. g-i. The interference pattern of the spoof SPPs and signal waves for designs 4-6.

Since the amplitude of the reference beam (spoof SPPs expressed in Eq. S38) and the objective wavefront in Eq.S39 are non-uniform, the maximum of interference pattern cannot be simply expressed by Eq. S25. Instead, the interference pattern is calculated by:

$$I(x) = |E_{\mathrm{sspp}} + E_0|^2, \tag{S40}$$

Using equations S38-S40, six designs are computed. The amplitude and phase distribution of the E_{sspp}, E_0, and the intensity profile of the interference pattern I(x) are shown in Supplementary Fig.21-22. Among them, designs 1-3 are the single-focusing designs with different off-axis offsets (0, 7 mm, 15 mm), designs 4-5 are the double-focusing designs with different off-axis offsets (7 mm, 15 mm), and design 6 is the triple-focusing design, wherein the off-axis offset is 15 mm.

We set the position of grooves on the top side as the coordinates of peaks in the interference pattern, while the depth (h_3 in Supplementary Fig.10) and width (t_3 in Supplementary Fig.10) of each groove are decided by the amplitude of the grooves:

$$\begin{cases} t_3 = t_{30} + p \cdot 10 \cdot dt_3 \\ h_3 = h_{30} + p \cdot 10 \cdot dh_3 \end{cases}, \tag{S41}$$

where p is the amplitude for each interference peak in Supplementary Fig.21g-i and Supplementary Fig.22g-i. t_{30}, h_{30}, dt_3, dh_3, and k_{sspp}, as well as t_2, h_2, and p_2 of coupling grooves, are optimized by the Nelder-Mead algorithm in COMSOL Multiphysics.

The structural parameters of designs 1-6 are listed in Supplementary Table 3-8. The simulated and measured intensity distributions in the xz-plane for each design are presented in Supplementary Fig.23. For better comparison, the simulated and measured intensity profiles at the focal plane for each design are given in Supplementary Fig.24. Although background noise and certain diffraction orders are observed in the experimental results, the designed focusing performance is preserved, and the FWHM of the measured focal line closely matches the simulation.

The top side images of samples for hologram of ‘4’, ‘7’, and ‘0’ are presented in Supplementary Fig.25a-c, respectively. The measured intensity distributions of y and x polarization for the hologram of ‘4’, ‘7’, and ‘0’ are presented in Supplementary Fig.25d-i. The holographic patterns in Fig. 4e-g are obtained by superpositioning the patterns of both polarizations in Supplementary Fig.25. All the other numbers can be achieved by combining the designs of 1-6.

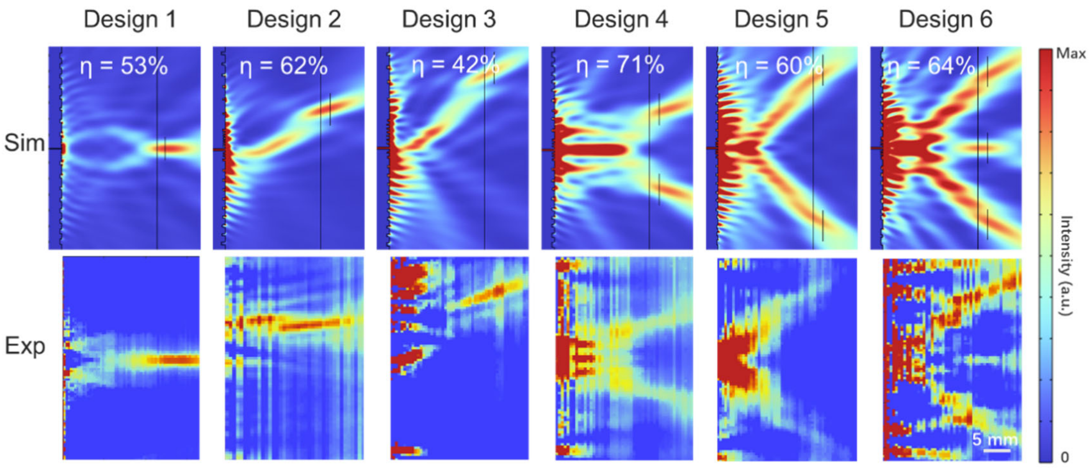

Supplementary Fig.23. Simulated and measured intensity profiles for designs 1-6.

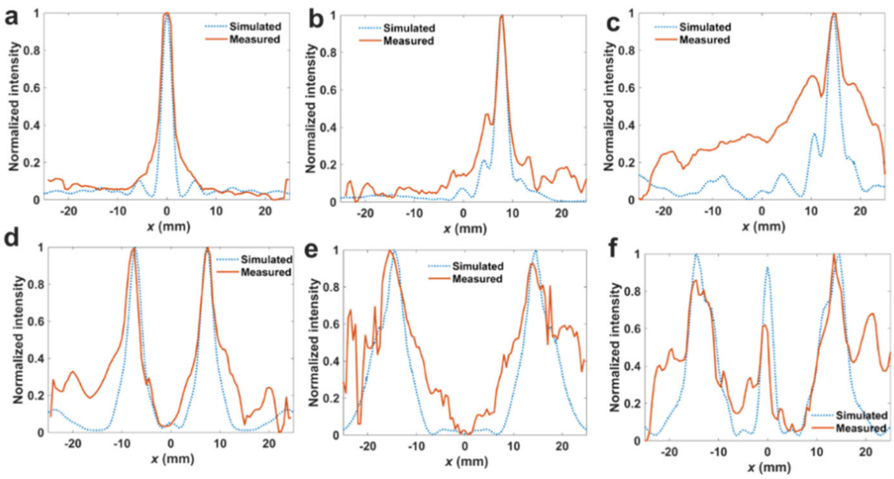

Supplementary Fig.24. Cross section of the intensity profile at the focal plane for the design 1-6

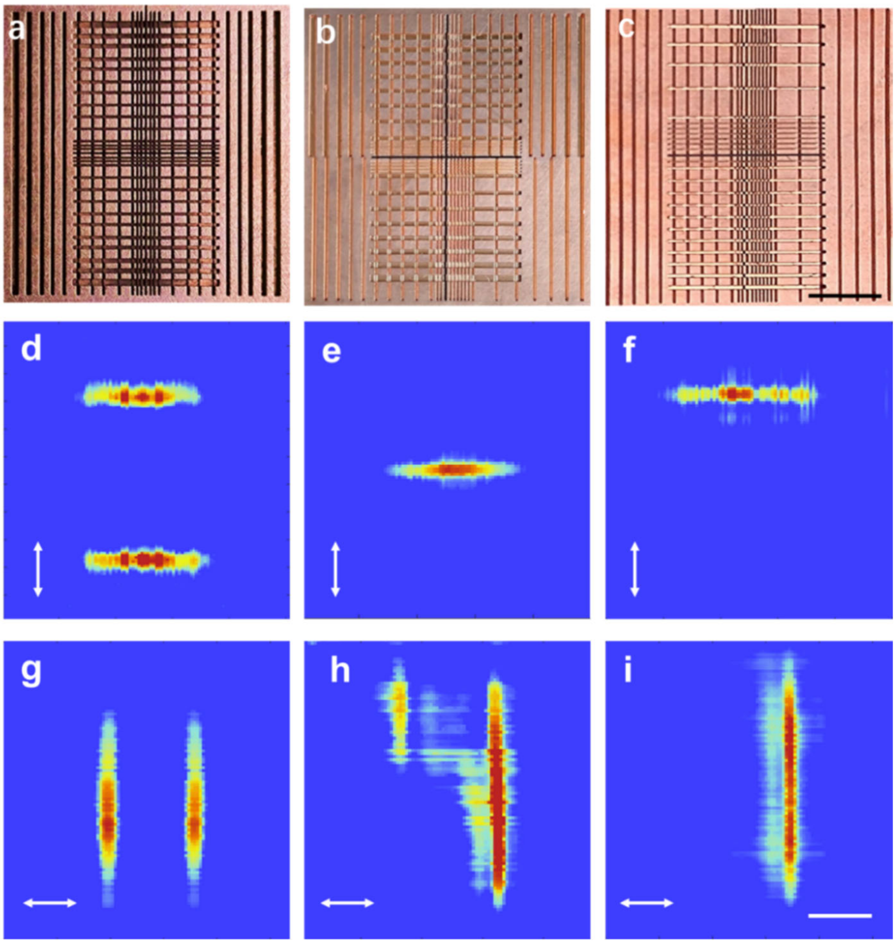

Supplementary Fig.25. Sample image (a-c) and intensity distribution of *y*-polarized (d-f) and *x*-polarized (g-i) light for the hologram of ‘4’, ‘7’, and ‘0’, respectively. Scale bar: 1 cm.

S.12 Design method and performance of spatially multiplexed thermal holography

For the spatial multiplexed design, the same grooves need to have different responses to incident surface waves excited at different WGs. The architecture of spatial multiplexed design is illustrated schematically in Supplementary Fig.26a. The design incorporates two WGs, and the excitation WG can be switched by blocking the other WG using a piece of copper tape (indicated by the yellow line in Supplementary Fig.26a). Regions R1 and R2 represent the scattering surfaces for WG 1 and WG 2, respectively. The central region C serves as the spatially multiplexed region for both WGs, designed to produce distinct wavefronts for surface waves excited by WG 1 and WG 2. By carefully optimizing the radiative loss, region C ensures that all surface waves excited by each WG are effectively scattered, minimizing crosstalk at R1 and R2. Additionally, coupling regions are designed on both sides of region C to enhance energy coupling from both WGs. The scattered wavefront for WGs can be expressed as:

$$E_{\mathrm{o}}(x)=\begin{cases} A_0\exp\left(ik_0\cdot\left(\sqrt{(x-x_1)^2+{f_1}^2}-f_1\right)+\psi_1\right), & \text{for slit 1} \\ A_0\exp\left(ik_0\cdot\left(\sqrt{(x-x_2)^2+{f_2}^2}-f_2\right)+\psi_2\right), & \text{for slit 2} \end{cases} \tag{S42}$$

where x_1, f_1, and ψ_1 are the offset of the focal line, focal length and biased phase for the wavefront excited by WG 1. x_2, f_2, and ψ_2 are the corresponding parameters for WG 2.

The artificially growing spoof SPPs field (reference beam) is expressed as:

$$E_{\mathrm{a,sspp}}(x)\begin{cases} = A_1\exp(\alpha x)\exp\left(ik_{\mathrm{sspp}}\cdot(x-x_{a1})+\varphi_1\right), & \text{for slit 1} \\ = A_1\exp(\alpha x)\exp\left(ik_{\mathrm{sspp}}\cdot(x-x_{a2})+\varphi_2\right), & \text{for slit 2} \end{cases} \tag{S43}$$

where x_{a1} and x_{a2} are the WG positions, and φ_1 and φ_2 are the biased phase for the spoof SPPs field excited by WG 1 and WG 2, respectively. The size and position of grooves can be obtained by the peaks of the interference pattern of $\mathrm{E_o}(x)$ and $\mathrm{E_{a,sspp}}(x)$.

Unlike the scattering surfaces designed in Supplementary Note S2 and S7, which serve a single scattering function, the multiplexed region C must satisfy two distinct holographic wavefronts, requiring additional design degrees of freedom. Parameters such as x_1, x_2, x_{a1}, x_{a2}, ψ_1, ψ_2, φ_1, φ_2, f_1, and f_2 are introduced to optimize the grooves in region C. The parameter range for x_1, x_2, x_{a1}, and x_{a2} is set as [-10 mm, -9 mm] or [9 mm, 10 mm] based on the side of WG position (for negative for WG 1 and positive for WG 2). The focal length range for f_1 and f_2 is [19 mm, 21 mm]. Narrow ranges for these parameters enable the design with sufficient optimization design degrees of freedom and desired scattering performance. For the biased phases, the range is [-π, π]. Particle swarm optimization (PSO) is applied for these parametric optimizations. The merit function in optimization is designed as:

$$\mathrm{err}=\begin{cases} \sum_k\left|x_{\mathrm{p1}}^k-x_{\mathrm{p2}}^k\right|, & \text{if } \left|x_{\mathrm{p1}}^k-x_{\mathrm{p2}}^k\right|<\lambda_0/10 \\ \mathrm{err}+\lambda_0\,, & \text{if } \left|x_{\mathrm{p1}}^k-x_{\mathrm{p2}}^k\right|\geq\lambda_0/10 \end{cases} \tag{S44}$$

where x_{p1}^k and x_{p2}^k are the k_{th} peaks in the interference pattern for the surface wave excited by WG 1 and WG 2, respectively. If the groove position can satisfy both wavefront tailoring functionalities ($\left|x_{\mathrm{p1}}^k-x_{\mathrm{p2}}^k\right|<\frac{\lambda_0}{10},\ \lambda_0=\ 3\ \mathrm{mm}$), the deviation of each groove is accumulated. If the groove position difference is larger than $\lambda_0/10$, a penalty factor of λ_0 is added to the merit function and this groove won't be sculpted in the final design. 1000 times of iteration in PSO are executed to minimize the merit function. The optimized amplitude and phase distribution of the scattered wave and spoof SPPs wave excited by WG 1 and WG 2 are plotted in Supplementary Fig.26b-e. The interference patterns are given in Supplementary Fig.26f. The optimized parameters for x_1, x_2, x_{a1}, x_{a2}, ψ_1, ψ_2, φ_1, φ_2, f_1 and f_2 are listed in Supplementary Table9. The groove sizes and positions on the top side are based on the peak position and amplitude of the interference pattern shown in Supplementary Fig.26f. The relationship between groove size and peak amplitude is are same as the Eq. S41. The groove size in the central region (C) is identical for both designs, with the value determined by the mean amplitude of the interference peaks in region C. Then, similar Nelder-Mead optimization in COMSOL Multiphysics is applied to optimize t_{30}, h_{30}, dt_3, dh_3, and k_{sspp}, as well as t_2, h_2, and p_2 of coupling grooves to achieve the highest focusing efficiency. Besides, since the size of region C is fixed after optimization, the grooves (t_{c1}, h_{c1}, p_{c1}) on the bottom in this region need to be redesigned to get the best coupling between surface wave and WG mode. The optimized structural parameters are given in Supplementary Table10. The simulated and measured emission performances of the sample, respectively exciting WG 1 and WG 2, are presented in Supplementary Fig.27a-d. Although background noise is observed in the experimental data, the wavefront switching functionality is well preserved. Supplementary Fig.27e-f shows the emitted patterns of different polarizations and corresponding blocking WGs.

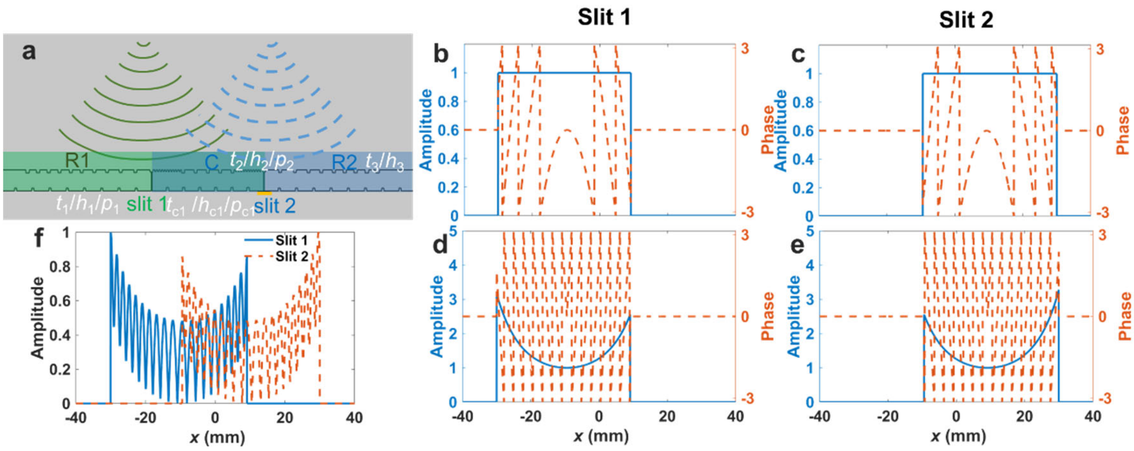

Supplementary Fig.26. Design of the spatial multiplexing device. a. Structural parameters in spatially multiplexed device. t_1, h_1, and p_1 are the width, depth, and period of the outer side grooves on the bottom surface (R1 and R2 regions). t_{c1}, $h_{c1}$and

p_{c1} are the width, depth, and period of the grooves on the bottom surface (C region). t_2, h_2 and p_2 are the width, depth, and period for the grooves in the coupling region on the top surface (C region) between the WG and the first groove of the radiative surface. t_3 and h_3 are the width and depth of the grooves in the radiative surface. A yellow solid line drawn at WG 2 represents a metal tape to shut the WG 2 off. Only WG 1 can be excited by the bottom surface, resulting in a single focusing profile (green solid waves) generated at R1 and C. On the contrary, blocking WG 1 could achieve another focusing profile (blue dashed waves) originating at R2 and C. The C region is spatially multiplexed for both focusing wavefronts. b-c. Amplitude and phase distribution for exciting WGs 1 and 2, respectively. d-e. The amplitude and phase of the diverging spoof SPPs for exciting WGs 1 and 2, respectively. f. The interference pattern of the spoof SPPs and signal waves are shown above for exciting WGs 1 and 2.

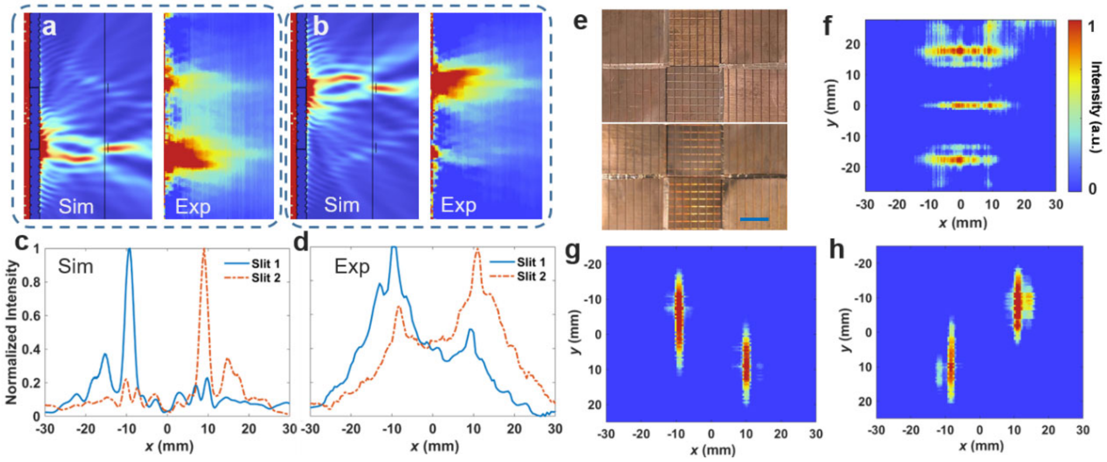

Supplementary Fig.27. Simulated and measured intensity distributions for the spatial multiplexing device. a-b. Simulated and measured intensity profiles by exciting WGs 1 and 2, respectively. c-d. Simulated and measured intensity profiles at the focal plane for WG 1 and 2 excitations, respectively. e. The sample picture and blocked WGs for holograms of ‘5’ and ‘2’. Scalar bar: 1 cm. f. Measured *x*-polarized intensity distribution for the spatial multiplexing device. g-h. Measured *y*-polarized intensity profiles for hologram ‘5’ and ‘2’ respectively.

S.13 Analysis of the emission performance with different spatial coherence

The spatial coherence of the surface wave on the top surface of our sample originates from the temporal coherence of the WG mode. By adjusting the WG width, the quality factor of the resonance can be tuned, as shown in Fig. 2c, resulting in varying spatial coherence of the surface wave on the top surface. To analyze the emission behavior of our design under different spatial coherence conditions, we fabricated several samples with varying WG widths but identical groove patterns on both surfaces. For a sample with a larger WG width (0.3 mm, $0.1\lambda_0$), the shorter temporal coherence leads to reduced spatial coherence of the surface waves. This results in a broader focal line for on-axis focusing emission and significantly higher-order focusing in off-axis focusing emission, as illustrated in Supplementary Fig.28. In contrast, the corresponding focusing performances with sufficient spatial coherence are demonstrated in Supplementary Fig.23 (Designs 1–3).

On the other hand, insufficient decay of the surface waves on the top surface can lead to excessive spatial coherence, which reduces the energy utilization efficiency of the surface waves. This effect is particularly evident in the spatially multiplexed design. As shown in Supplementary Fig.29, when one WG is excited, the surface waves can also excite the other WG, introducing crosstalk between the functionalities of the two WGs.

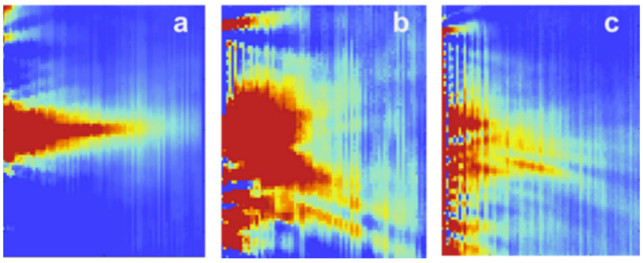

Supplementary Fig.28. Measured intensity profile for the devices with limited spatial coherence. A broader focal line for on-axis focusing emission (a) and significant high-order focusing in off-axis focusing emission (b-c) is obtained compared with the Design 1-3 results shown in Supplementary Fig.23.

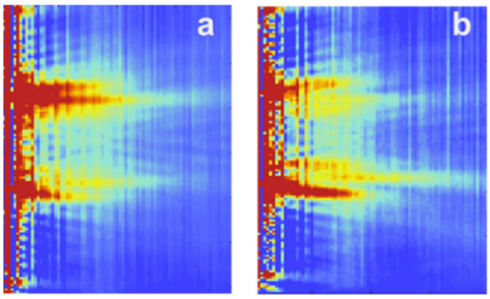

Supplementary Fig.29. Measured intensity profile for the spatial multiplexing device with extreme spatial coherence. Insufficient decay of grooves results in the insufficient energy utilization of surface waves, which can be obtained in the unwanted wavefront in spatial multiplexed design.

S.14 Analysis for the inner-cavity WG design and device with ultra-large coherent size

The mode lifetime (quantified by the Q-factor $\tau = Q/\omega$) of the proposed WG in the main text (Fig. 2c) is primarily determined by two loss mechanisms: radiation loss (γ_r) governed by WG width, and absorption loss (γ_i) dominated by current density at metallic boundaries. Narrowing the WG width reduces γ_r while simultaneously increasing electromagnetic energy density within the confined mode volume. This intensified field concentration elevates surface current densities at metal walls, consequently enhancing γ_i through Ohmic dissipation. The γ_r and γ_i can be partially decoupled by introducing an expanded central chamber (width w_2) in the WG structure (CHW: cavity hybrid waveguide mode), as Supplementary Fig.30a shown. By maintaining constant WG exit width w_1 (thus fixed γ_r), this architectural modification significantly enlarges the mode volume within the chamber region. The resultant reduction in EM energy density along the metal wall directly suppresses γ_i through diminished surface current densities. To satisfy resonance conditions, both WG and chamber length must obey half-wavelength quantization: $l_1 = m\lambda_0/2$ and $l_2 = n\lambda_0/2$, where $m,n \in \mathbb{Z}^+$.

Supplementary Fig.30b presents the mode lifetime dependence on geometric parameters w_1 and w_2. The lifetime exhibits monotonic growth with chamber width w_2, while reaching saturation at $w_1 \approx \lambda_0/1000$, where WG exit absorption becomes the dominant loss mechanism. While larger w_2 value generally enhances mode lifetime, dimensional constraints emerge at $w_2 > \lambda_0$ where higher-order chamber modes develop (Supplementary Fig.30a,c-e). These parasitic modes (C_1HW and C_2HW in Supplementary Fig.30a) dramatically degrade cavity transmission, with optimal performance achieved at $w_2 \approx \lambda_0/2$. This configuration enables a remarkable mode lifetime enhancement to $4000\tau_0$ ($w_1 = \lambda_0/1000$, $l_1 = \lambda_0$, $l_2 = \lambda_0/2$). Strong coupling between the surface wave and the inner-cavity assisted WG is reflected in the high transmission efficiency of the device and the eigenmode of the whole device, as shown in Supplementary Fig.30f, h. The spatial coherence and cross-spectral density component W_{zz} of the top surface mode as a function of propagation distance are given in Supplementary Fig.30g and i. Optimal w_1 enables extraordinary coherence extension up to $1000\lambda_0$. Comparative studies reveal distinct coherence behaviors: BM and W-RM maintain near-constant W_{zz} across simulated distances, whereas S-RM demonstrates rapid decay with $1/\sqrt{e}$ attenuation occurring at $\sim 12\lambda_0$ - consistent with theoretical predictions in Supplementary Fig.30g.

Limited by the computational capability, DF meta-emitter with $100\lambda_0$ coherent size are demonstrated here. BM and W-RM are configured as the bottom and top surface modes, respectively, with inner-cavity WG tunnel to design the thermal oblique emission, self-focusing and holography devices. Applying the design strategy from the *Self-Focusing Thermal Emission* section (Main Text), we obtain an oblique emission device (Design 7) and a self-focusing device (Design 8) both with $100\lambda_0$ coherent size, whose eigenmode profiles are shown in Supplementary Fig.31a and Fig. 32, respectively. For Design 7, Supplementary Fig.31b displays the H_y component of eigenmode where tilted iso-phase contours indicate obliquely emitted plane waves, while Supplementary Fig.31c shows its far-field diffraction pattern featuring a distinct lobe with full width of half maximum (FWHM) around 0.7°, which implies $\sim 100\lambda_0$ coherent size. For Design 8, the focal intensity cross-section (left panel) reveals a near diffraction-limited spot (FWHM$\approx 0.8\lambda_0$) at the target plane, confirming ultra-large spatial coherence along the surface, as shown in Supplementary Fig.32. Similarly, by implementing the design scheme presented in Supplementary Note S11, thermal holography with spatial coherence of $100\lambda_0$ can be also achieved. We design the thermal holographic pattern '8' as example. The amplitude and phase distribution of the E_{sspp}, E_0, and the intensity profile of the interference pattern $I(x)$ for triple focusing (Design 9) and double off-axis focusing (Design 10) are shown in Supplementary Fig.33-34, respectively. The eigenmode profiles of the corresponding designs are presented in Supplementary Fig.35. The eigenmode profiles exhibit surface wave coupling across both interfaces and target far-field scattering. The structural information of Design 7-10 can be found in the Supplementary Table.11-14.

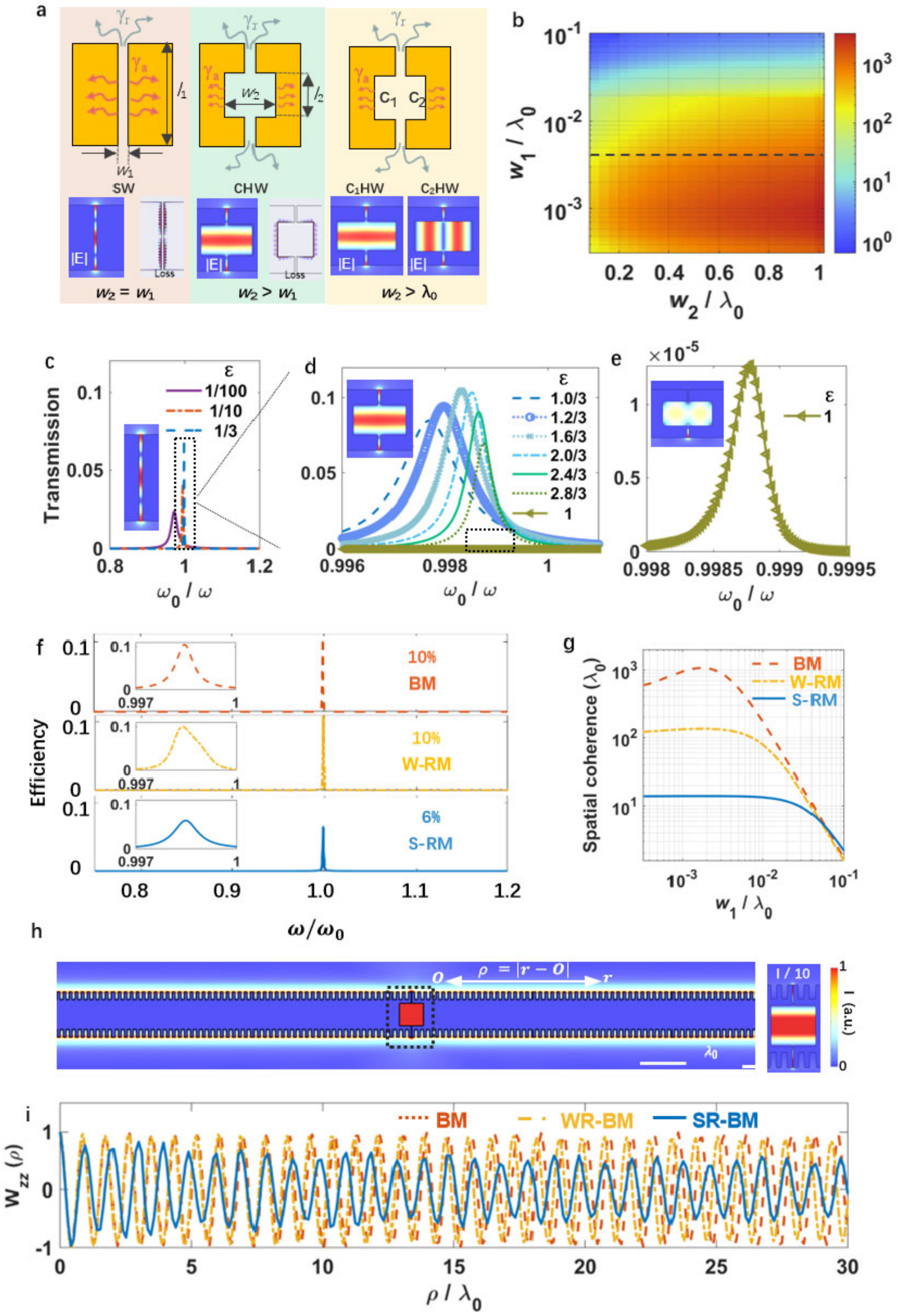

Supplementary Fig.30. Analysis for the inner-cavity WG design. a. Geometric sketches of the WG cavities with different center width w_2 and corresponding eigenmode profiles and distribution of power loss density. γ_r and γ_i represent radiation loss and absorption loss, respectively. c_1 and c_2 denote two resonance modes in the cavity. SW: slit waveguide; CHW: cavity hybrid mode. b. The mode lifetime ($\tau = Q/\omega$, $\tau_0 = 2\pi/\omega_0$) as a function of w_1 and w_2. $l_1 = \lambda_0$ and $l_2 = \lambda_0/2$ are set in the simulation. c-e. The transmission spectrum for different normalized center width $\varepsilon = w_2 / \lambda_0$. The electric field at resonance peak is given in the inset. In the simulation, $w_1 = \lambda_0/150$, $l_1 = \lambda_0$ and $l_2 = \lambda_0/2$. d and e are the enlarged spectrum regions marked by the dash box in c and d, respectively. f. Energy tunnelling efficiencies of the hybrid mode with BM on the bottom surface and BM, W-RM and S-RM on the top surface. $l_1 = \lambda_0$, $l_1 = \lambda_0$, $w_1 = \lambda_0/300$, $w_2 = 0.8\lambda_0$ are set in the simulation. g. Spatial coherence of different surfaces as a function of the w_1, $w_2 = 0.8\lambda_0$ is set in the simulation. h. Eigenmode profile of the DF meta-emitter. The BM is configured as both the bottom and top structures in the simulation. Here, ***O*** and ***r*** represent the coordinates of the WG and an arbitrary point on the top surface, while ρ denotes the distance between these two points. The enlarged view of the center WG cavity is shown on the right side with rescaled intensity to clearly show the mode pattern. i. Cross-spectral density component $W_{zz}(\rho)$ of the surface wave as a function of ρ at fixed height $z_0 = \lambda_0/10$ above the surface.

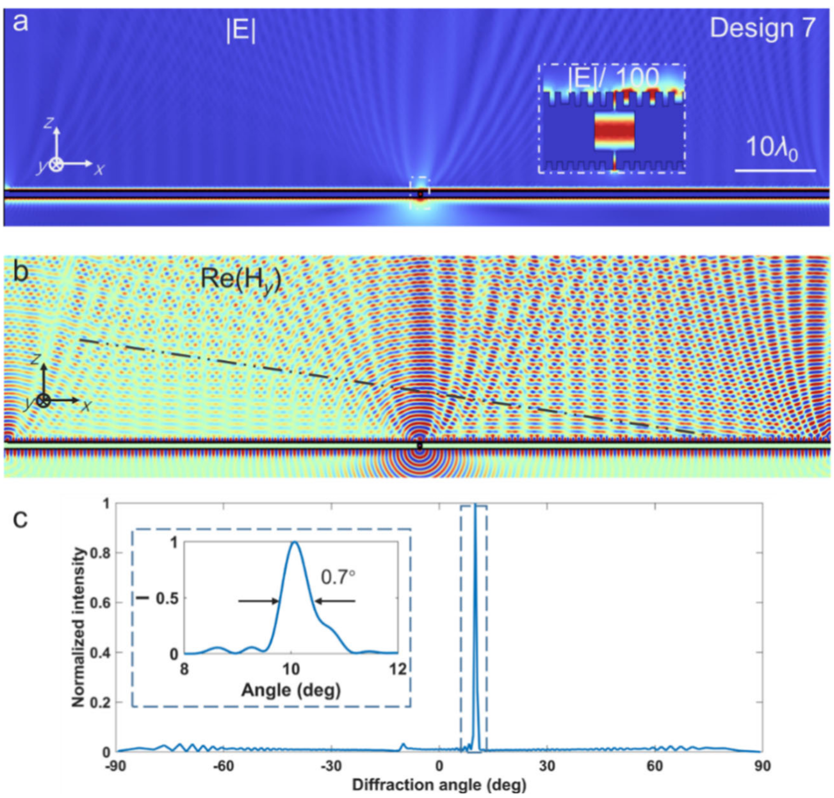

Supplementary Fig.31. Plane wave emission device (design 7). a. Eigenmode profile (emission angle: 10°). Inset: Magnified view of center dashed region with rescaled intensity revealing inner-cavity WG mode pattern. b. Real part distribution of H_y component. Phase profile is denoted by black dash-dotted line. c. Far-field diffraction pattern. Inset: Enlarged dashed-rectangle region showing main lobe. (FWHM $\approx$ 0.7°)

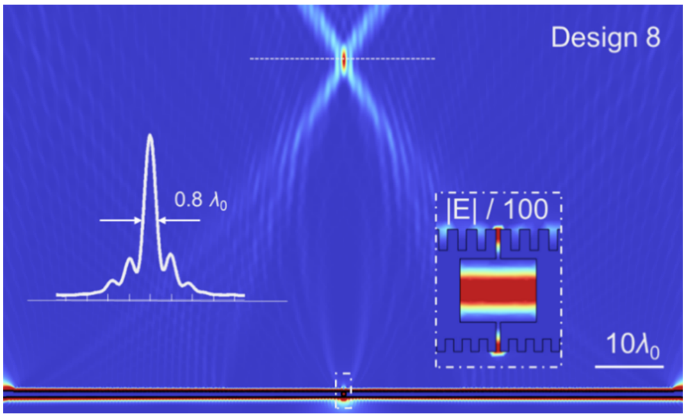

Supplementary Fig.32. Eigenmode profile of the design 8. Inset: Enlarged view of the white dashed region, with the intensity rescaled to clearly display the inner-cavity WG mode pattern. The cross-section of focal intensity profile is plotted in the left side, with FWHM marked on the profile.

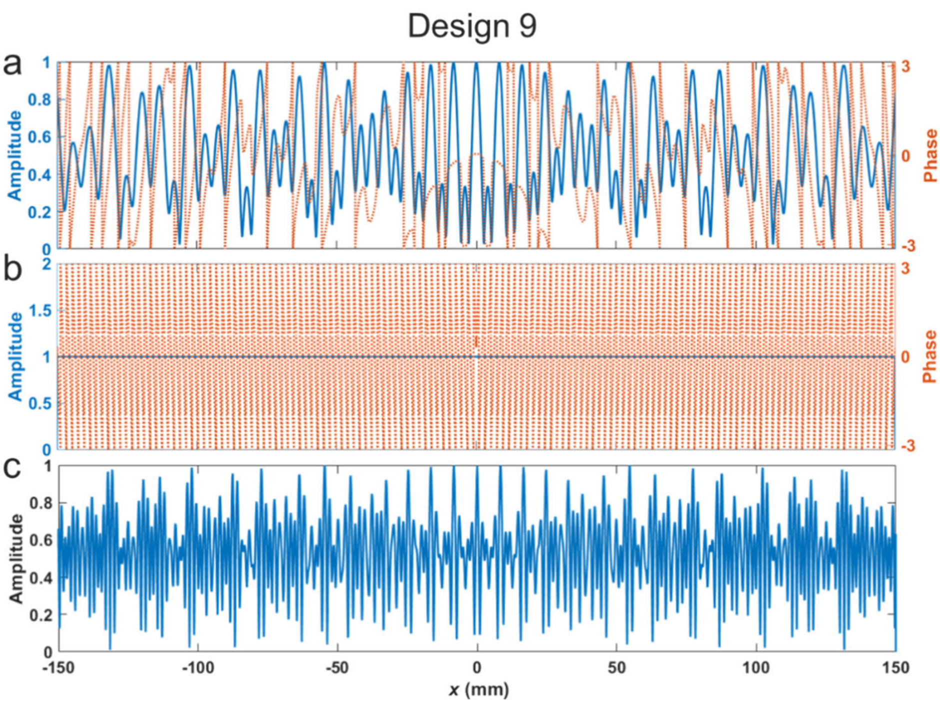

Supplementary Fig.33. Design of the holographic design 9. a. Amplitude and phase distribution. b. The amplitude and phase of the diverging spoof SPPs. c. The interference pattern of the spoof SPPs and signal waves.

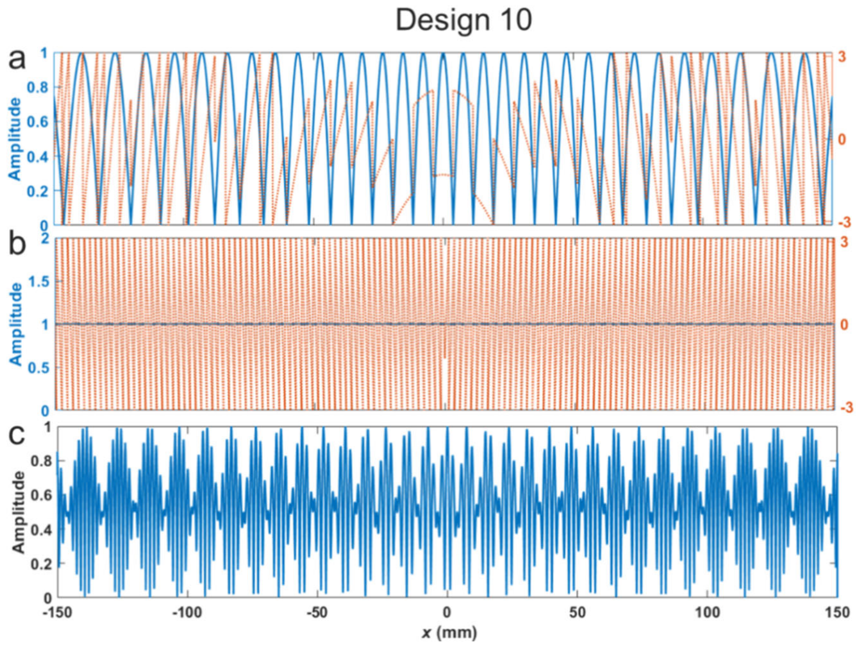

Supplementary Fig.34. Design of the holographic design 10. a. Amplitude and phase distribution. b. The amplitude and phase of the diverging spoof SPPs. c. The interference pattern of the spoof SPPs and signal waves.

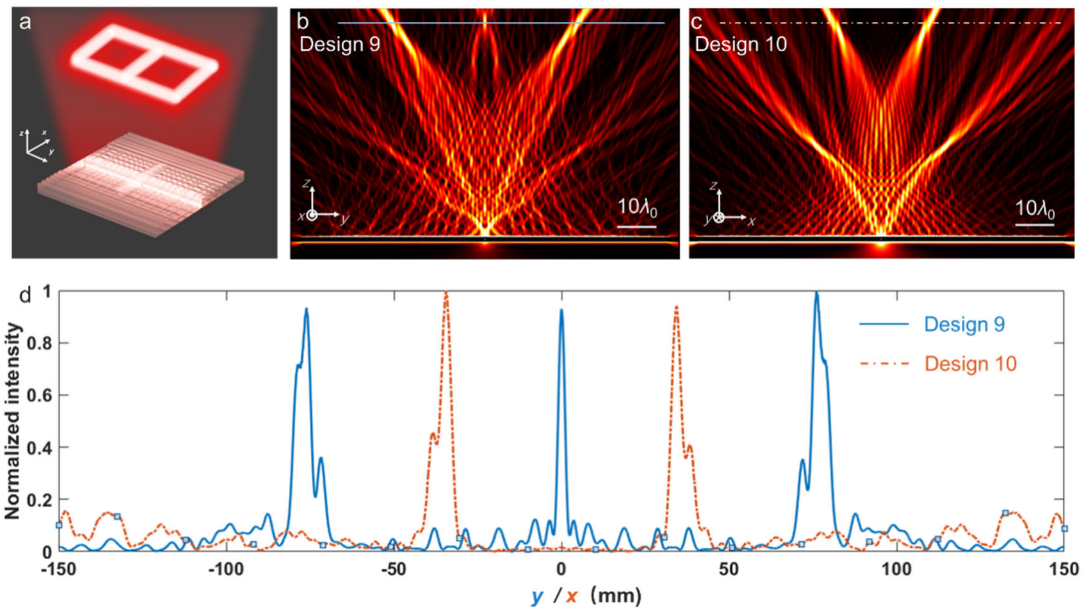

Supplementary Fig.35. Thermal hologram for the device with 100λ_0 coherent size. a. Schematic diagram of the hologram of "8". b-c. Eigenmode profile of the design 8-9. d. The cross-section of focal intensity profile of design 8-9. The focal plane is marked in the corresponding figure.

S.15 2D design for the radially polarized focusing emission

In addition to the 1D and quasi-2D thermal wavefront engineering devices demonstrated in the previous section, true 2D thermal wavefront tailoring functionality could also be achieved using DF meta-emitter. By incorporating an axially symmetric bull's eye structure on the bottom surface and utilizing the proposed holographic pattern generation approach, more sophisticated emission wavefronts can be obtained. As a proof-of-concept, a radially polarized focusing emission design is proposed. Supplementary Fig.36a-b schematically shows the top surface and the axial cross-section of the design. Similar to the proposed WG mode, the center tiny hole also acts as a cavity and exhibits a single resonance within the designed band. To increase the in-plane wavevector of the scattered field at the exit of the hole, an Aluminum oxide (Al_2O_3, refractive index n = 3.24) ceramic rod is designed in the center hole.

The long-lifetime cavity mode is converted to the radially diverging surface mode on the top surface and is scattered out at the designed position. The radially propagating surface wave leads to the focal spot naturally having a radially polarized behavior, as illustrated in Supplementary Fig.36b. The intensity profiles of focal spots for each polarization are given in Supplementary Fig.36c, and the final donut-shaped focal spot is shown in Supplementary Fig.36d, which exhibits the radial polarization property. The structural parameters in this design are listed in Supplementary Table15. With the holographic design, a more sophisticated pattern can be achieved by this architecture[21].

In comparison to the long WG design presented in the main text, the axially symmetric bull's eye structure, featuring a central hole, imposes additional constraints on device transmission, presenting notable detection challenges. Although increasing the hole size could potentially enhance transmission, this modification risks exciting higher-order modes within the operational band, which would generate substantial undesirable background noise. Through careful optimization of the coupling between the bottom surface's spoof SPPs and the hole cavity, combined with the implementation of critical coupling to balance radiative and absorption losses, both the transmission characteristics and the overall efficiency of the device can be further improved.

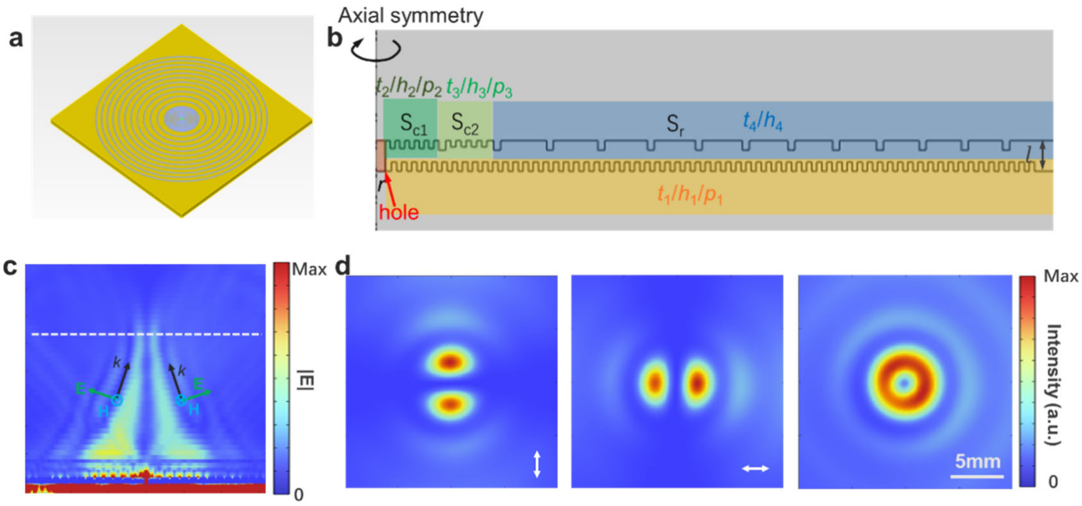

Supplementary Fig.36. Focused radially polarized thermal emission design. a. Schematic diagram of the sample with radially polarized focusing emission behavior. b. Axial cross-section of the design. The axial symmetry line is the left boundary in the figure. The red region denotes the center hole (radius is *r*), which is filled with an Aluminum oxide (Al_2O_3, refractive index n = 3.24) ceramic rod to increase the in-plane wavevectors of the scattered field at the exit of the hole. t_1, h_1, and p_1 are the width, depth, and period of the grooves on the bottom surface (yellow region). t_2, h_2, and p_2 are the width, depth, and period of the grooves in the first coupling surface (S_{c1}, green region on the top surface) between the hole and the first scattering groove. t_3, h_3, and p_3 are the width, depth, and period for the grooves in the second coupling surface (S_{c1}, light green region on the top surface) between the first and second groove of the radiative surface. t_4 and h_4 are the width and depth of the grooves in the radiative surface (S_r, blue region). c. A cross-sectional |E| profile of the designed device. The electric and magnetic fields of the scattering wave, along with the wavevector, are denoted by the arrows in the figure. d. The intensity profiles for *y*-polarized, *x*-polarized, and the superposition of both polarized light at the focal plane.

S.16 Self-focusing thermal meta-emitter at mid-infrared

In the mid-IR, increased metallic loss leads to higher absorption for both the spoof surface plasmon polariton (SSPP) mode and the connecting slit waveguide. In the demonstrated millimeter-wave regime, the conductivity of copper is taken as $\sigma = 5.8 \times 10^7$ S/m at a wavelength of 3 mm. By comparison, in the mid-IR, gold exhibits complex refractive index **n** = $n + ik = 2 + 39i$ at $\lambda = 5.8$ μm, corresponding to an effective conductivity of $\sigma = 2nk\omega\varepsilon_0 \approx 4.6\times10^5$ S/m.

For the surface mode, the increased absorption loss can be partially mitigated by employing a low-confinement configuration, such as the S-RM mode discussed in the main text. We simulated a structure scaled by a factor of 600 operating in the mid-IR. In this case, the Q factor decreases from 98 to 81, corresponding to only a 17% degradation in temporal coherence. The group velocity remains high ($\approx 0.93c$), comparable to that of the original design, while the spatial coherence degradation is also limited to approximately 17%. Furthermore, the temporal decay of the scaled mode can be compensated by further reducing the size of the radiative grooves (perturbations), thereby maintaining a low radiative decay rate for the surface mode.

For the slit waveguide, the Q factor decreases from 31 to 21, which primarily affects the spatial coherence of emission from the top surface. This radiative loss can be substantially suppressed through geometric optimization of the slit, for example by enlarging the chamber region to reduce electromagnetic energy density near the metal walls. This mechanism is discussed in detail in Supplementary Note S14 and Supplementary Fig.30.

By applying a similar design strategy, a self-focusing meta-emitter operating at 5.7 μm can be readily realized, as demonstrated in Supplementary Fig.37b. The dispersion of the refractive index of gold is plotted in Supplementary Fig.37a. The scaled device maintains single-mode properties within the designed band (2–10 μm), as shown in Supplementary Fig.37c. The cross-sectional intensity profile at the focal plane is illustrated in Supplementary Fig.37d. The FWHM is approximately 3.6 μm, close to the diffraction limit (~3.1 μm), indicating strong spatial coherence along the surface.

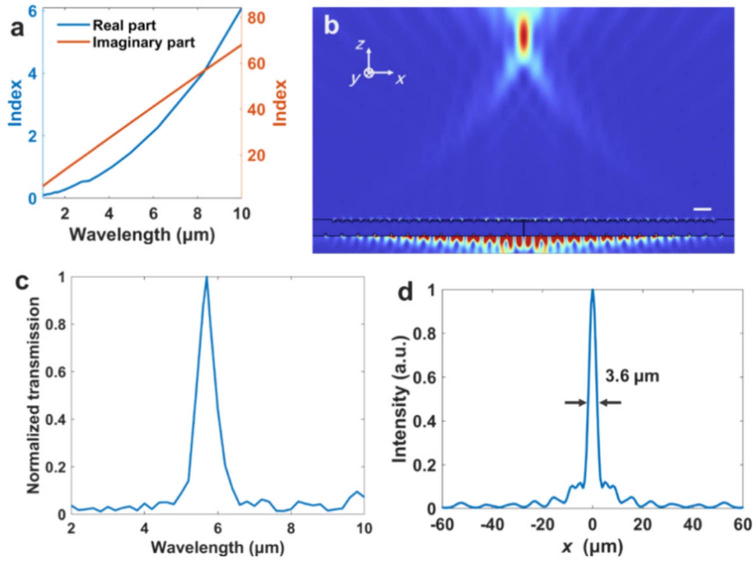

Supplementary Fig.37. Self-focusing thermal emission design at mid-infrared band. a. Real and imaginary parts of the refractive index of gold used in simulation. b. The eigenmode profile of the designed structure. Scalar bar: 5 μm. c. Normalized transmission of the device with plane wave excitation. d. The cross-section of the focal spot. The FWHM is marked in the plot.

Supplementary Tables:

Supplementary Table1 Comparison with advanced thermal manipulation techniques

	L_c/λ_0	Sim/ Exp	Rainbow -free	Directional emission	Focusing	Holo- graph y	Ref.
SiC grating	60	Exp	×	√	×	×	1
2D SiC grating	~20	Exp	√	√	×	×	2
Micro-emitter	Not reported	Exp	×	√	×	×	24
Coupled cavity	32	Exp	×	√	×	×	6
Bull's eye structure	47	Exp	×	√	×	×	4
Shallow W grating	24	Exp	×	√	×	×	5
MIM resonator	<10	Exp	×	√	×	×	7
Quasi-Bound Modes	75.5	Exp	×	√	×	×	8
Distorted photonics	Not reported	Exp	√	√	×	×	9
Monoclinic grating	<20	Exp	√	√	×	×	10
Ternery grating	~50	Exp	√	√	×	×	11
Thermal metasurface-single layer	1.6	Exp	√	√	×	×	16
SiC surface	~60	Sim	√	×	Partially focusing	×	3

Mesoscopic resonator	~20	Sim	√	×	√	√	12
Thermal metasurface-double layer	~8	Sim	×	√	√	√	14
Meta-emitter	**11**	**Exp**	**√**		**√**	**√**	**This work**
Meta-emitter	**100**	**sim**	**√**	**√**	**√**	**√**	**This work**

Supplementary Table2 The parameter values of the 1D self-focusing emission design.

parameter	Value (mm)	parameter	Value (mm)
t_1	0.35	p_2	0.45
h_1	0.4	t_3	0.376
p_1	2.88	h_3	0.483
k_{sspp} / k_0	1.15 (dimensionless)	t_4	0.22
w	0.1	h_4	0.308
l	2.9	dh_4	0.046
t_2	0.2	p_4	0.52
h_2	0.4		

Supplementary Table3 Structural parameters for the groove on the top side in design 1

parameter	Value (mm)	parameter	Value (mm)
t_2	0.25	t_{30}	0.341
h_2	0.15	h_{30}	0.373
p_2	0.47	dt_3	0.081
dh	0	dh_3	0

Supplementary Table4 Structural parameter for the groove on the top side in design 2

parameter	Value (mm)	parameter	Value (mm)
t_2	0.25	t_{30}	0.25
h_2	0.45	h_{30}	0.35
p_2	0.48	dt_3	0.035
dh	0	dh_3	0.01

Supplementary Table5 Structural parameters for the groove on the top side in design 3

parameter	Value (mm)	parameter	Value (mm)
t_2	0.25	t_{30}	0.31
h_2	0.4	h_{30}	0.31
p_2	0.7	dt_3	0.03
dh	0	dh_3	0.02

Supplementary Table6 Structural parameters for the groove on the top side in design 4

parameter	Value (mm)	parameter	Value (mm)
t_2	0.25	t_{30}	0.25
h_2	0.42	h_{30}	0.406
p_2	0.5	dt_3	0.095
dh	0	dh_3	0.014

Supplementary Table7 Structural parameters for the groove on the top side in design 5

parameter	Value (mm)	parameter	Value (mm)
t_2	0.28	t_{30}	0.25
h_2	0.445	h_{30}	0.372
p_2	0.45	dt_3	0.106
dh	0	dh_3	-0.015

Supplementary Table8 Structural parameters for the groove on the top side in design 6

parameter	Value (mm)	parameter	Value (mm)
t_2	0.25	t_{30}	0.437
h_2	0.45	h_{30}	0.34

p_2	0.55	dt_3	0.153
dh	0	dh_3	0

Supplementary Table9 Parameters for the wavefront design in the spatially multiplexed sample

parameter	Value	parameter	Value
x_1	9.36 mm	ψ_2	-0.03π
x_2	-9.67 mm	φ_1	0.11π
x_{a1}	9.11 mm	φ_2	0.11π
x_{a2}	-9.46 mm	f_1	19.16 mm
ψ_1	-0.03π	f_2	20.58 mm

Supplementary Table10 Structural parameters for the spatially multiplexed sample

parameter	Value (mm)	parameter	Value (mm)
t_1	0.35	t_2	0.2
h_1	0.4	h_2	0.22
p_1	2.88	p_2	0.445
t_{c1}	0.41	t_{30}	0.35
h_{c1}	0.482	h_{30}	0.34
p_{c1}	2.66	dt_3	0.125
k_{sspp} / k_0	1.06 (dimensionless)	dh_3	0.043

Supplementary Table11 The parameter values of the design 7 with 100 λ_0 coherent size.

parameter	Value (mm)	parameter	Value (mm)
t_1	0.2	t_3	0.3
h_1	0.3	h_3	0.45
p_1	0.4	t_4	0.2

k_{sspp} / k_0	1.4 (dimensionless)	h_4	0.435
w	0.1	dh_4	0.1
l	2.9	p_4	0.5

Supplementary Table12 The parameter values of the design 8 with 100 λ_0 coherent size.

parameter	Value (mm)	parameter	Value (mm)
t_1	0.2	p_2	0.45
h_1	0.3	t_3	0.3
p_1	0.4	h_3	0.45
k_{sspp} / k_0	1.4 (dimensionless)	t_4	0.2
w	0.1	h_4	0.435
l	2.9	dh_4	0.1
t_2	0.2	p_4	0.5
h_2	0.3		

Supplementary Table13 The parameter values of the design 9 with 100 λ_0 coherent size.

parameter	Value (mm)	parameter	Value (mm)
t_1	0.2	h_{30}	0.35
h_1	0.3	dt_3	0.015
p_1	0.4	dh_3	0.01
k_{sspp} / k_0	1.4 (dimensionless)	t_4	0.2
w	0.1	h_4	0.435
l	3.25	dh_4	0.1
t_{30}	0.22	p_4	0.5

Supplementary Table14 The parameter values of the design 10 with 100 λ_0 coherent size.

parameter	Value (mm)	parameter	Value (mm)
t_1	0.2	h_{30}	0.35
h_1	0.3	dt_3	0.014
p_1	0.4	dh_3	0.011
k_{sspp} / k_0	1.4 (dimensionless)	t_4	0.2
w	0.1	h_4	0.435
l	3.25	dh_4	0.1
t_{30}	0.22	p_4	0.5

Supplementary Table15 The parameter values of the 2D radially polarized focusing emission design.

parameter	Value (mm)	parameter	Value (mm)
t_1	0.26	t_3	0.25
h_1	0.45	h_3	0.304
p_1	0.491	p_3	0.5
t_2	0.24	t_4	0.33
h_2	0.382	h_4	0.45
p_2	0.47	dt_3	0.125
k_{sspp} / k_0	1.06 (dimensionless)	n_{core}	3.24 (dimensionless)
r	0.453	l	1.5

Supplementary Reference:

1. Greffet, J.-J. *et al.* Coherent emission of light by thermal sources. *Nature* **416**, 61–64 (2002).
2. Arnold, C. *et al.* Coherent thermal infrared emission by two-dimensional silicon carbide gratings. *Phys. Rev. B* **86**, 035316 (2012).
3. Chalabi, H., Alù, A. & Brongersma, M. L. Focused thermal emission from a nanostructured SiC surface. *Phys. Rev. B* **94**, 094307 (2016).
4. Park, J. H., Han, S. E., Nagpal, P. & Norris, D. J. Observation of Thermal Beaming from Tungsten and Molybdenum Bull's Eyes. *ACS Photonics* **3**, 494–500 (2016).
5. Laroche, M. *et al.* Highly directional radiation generated by a tungsten thermal source. *Opt. Lett.* **30**, 2623 (2005).
6. Dahan, N. *et al.* Enhanced coherency of thermal emission: Beyond the limitation imposed by delocalized surface waves. *PHYSICAL REVIEW B* **76**, 045427 (2007).
7. Lochbaum, A. *et al.* Compact Mid-Infrared Gas Sensing Enabled by an All-Metamaterial Design. *Nano Lett.* **20**, 4169–4176 (2020).
8. Sun, K., Levy, U. & Han, Z. Exploiting Zone-Folding Induced Quasi-Bound Modes to Achieve Highly Coherent Thermal Emissions. *Nano Lett* **24**, 764–769 (2023).
9. Sun, K., Cai, Y., Huang, L. & Han, Z. Ultra-narrowband and rainbow-free mid-infrared thermal emitters enabled by a flat band design in distorted photonic lattices. *Nat Commun* **15**, 4019 (2024).
10. Sun, K., Yang, B., Cai, Y., Kivshar, Y. & Han, Z. Circularly polarized thermal emission driven by chiral flatbands in monoclinic metasurfaces. *Sci. Adv.* **11**, eadw0986 (2025).
11. Wang, K. *et al.* High-Q Resonance Engineering in Momentum Space for Highly Coherent and Rainbow-Free Thermal Emission. *Nano Lett.* **25**, 3613–3619 (2025).
12. Zhou, M. *et al.* Self-Focused Thermal Emission and Holography Realized by Mesoscopic Thermal Emitters. *ACS Photonics* **8**, 497–504 (2021).
13. Cui, T.-J., Liu, S. & Li, L.-L. Information entropy of coding metasurface. *Light Sci Appl* **5**, e16172–e16172 (2016).
14. Overvig, A. C., Mann, S. A. & Alù, A. Thermal Metasurfaces: Complete

Emission Control by Combining Local and Nonlocal Light-Matter Interactions. *Phys Rev X* **11**, 021050 (2021).
15. Fan, S., Suh, W. & Joannopoulos, J. D. Temporal coupled-mode theory for the Fano resonance in optical resonators. *J. Opt. Soc. Am. A* **20**, 569 (2003).
16. Nolen, J. R., Overvig, A. C., Cotrufo, M. & Alù, A. Local control of polarization and geometric phase in thermal metasurfaces. *Nat. Nanotechnol.* **19**, 1627–1634 (2024).
17. Sun, K. *et al.* Full polarization and high coherence control of thermal emissions via saddle-band dispersion engineering. *Nat. Commun.* **16**, 8393 (2025).
18. Janssen, O. T. A., Urbach, H. P. & ’T Hooft, G. W. Giant Optical Transmission of a Subwavelength Slit Optimized Using the Magnetic Field Phase. *Phys. Rev. Lett.* **99**, 043902 (2007).
19. Wonjoo Suh, Zheng Wang, & Shanhui Fan. Temporal coupled-mode theory and the presence of non-orthogonal modes in lossless multimode cavities. *IEEE J. Quantum Electron.* **40**, 1511–1518 (2004).
20. Komisar, D. *et al.* Multiple channelling single-photon emission with scattering holography designed metasurfaces. *Nat Commun* **14**, 6253 (2023).
21. Chen, Y.-H., Huang, L., Gan, L. & Li, Z.-Y. Wavefront shaping of infrared light through a subwavelength hole. *Light Sci Appl* **1**, e26–e26 (2012).
22. Yu, N. *et al.* Designer spoof surface plasmon structures collimate terahertz laser beams. *Nature Mater* **9**, 730–735 (2010).
23. Wolf, E. *Introduction to the Theory of Coherence and Polarization of Light*. (Cambridge University Press, 2007).
24. Fan, Z., Hwang, T., Lin, S., Chen, Y. & Wong, Z. J. Directional thermal emission and display using pixelated non-imaging micro-optics. *Nat Commun* **15**, 4544 (2024).